



## Dipolar and contact paramagnetic NMR chemical shifts in $\text{An}^{IV}$ complexes with dipicolinic acid derivatives

Md. Ashraful Islam, Matthieu Autillo, Laetitia Guérin, Christelle Tamain, Philippe Moisy, Hélène Bolvin, Claude Berthon

### ► To cite this version:

Md. Ashraful Islam, Matthieu Autillo, Laetitia Guérin, Christelle Tamain, Philippe Moisy, et al.. Dipolar and contact paramagnetic NMR chemical shifts in  $\text{An}^{IV}$  complexes with dipicolinic acid derivatives. *Inorganic Chemistry*, 2022, 61 (27), pp.10329-10341. 10.1021/acs.inorgchem.2c00845 . hal-03766320

**HAL Id: hal-03766320**

**<https://hal.science/hal-03766320v1>**

Submitted on 31 Aug 2022

**HAL** is a multi-disciplinary open access archive for the deposit and dissemination of scientific research documents, whether they are published or not. The documents may come from teaching and research institutions in France or abroad, or from public or private research centers.

L'archive ouverte pluridisciplinaire **HAL**, est destinée au dépôt et à la diffusion de documents scientifiques de niveau recherche, publiés ou non, émanant des établissements d'enseignement et de recherche français ou étrangers, des laboratoires publics ou privés.

# Dipolar and contact paramagnetic chemical shifts in $An^{IV}$ complexes with dipicolinic acid derivatives.

*Md. Ashraful Islam<sup>‡</sup> Matthieu Autillo<sup>†</sup> Laetitia Guérin<sup>†</sup> Christelle Tamain<sup>†</sup> Philippe Moisy<sup>†</sup>  
Hélène Bolvin,<sup>\*,‡</sup> and Claude Berthon<sup>\*,†</sup>*

<sup>†</sup> CEA, DES, ISEC, DMRC, Univ. Montpellier, Marcoule, France.

<sup>‡</sup> Laboratoire de Chimie et Physique Quantiques, CNRS, Université Toulouse III, 118 Route de Narbonne, 31062 Toulouse, France.

\* corresponding authors

KEYWORDS. Actinide, paramagnetic NMR spectroscopy, Bleaney's theory, *ab initio* calculations, covalency.

ABSTRACT. Actinide +IV complexes ( $An^{IV} = Th^{IV}, U^{IV}, Np^{IV}$  and  $Pu^{IV}$ ) with two dipicolinic acid derivatives (DPA and Et-DPA) have been studied by  $^1H$  and  $^{13}C$  NMR spectroscopy and first-principles calculations. The Fermi contact and dipolar contributions to the Actinide Induced Shifts (AIS) are evaluated from a temperature dependence analysis, combined with *ab initio* results. It allows an experimental estimation of the axial anisotropy of the magnetic susceptibility  $\Delta\chi_{ax}$  and of the hyperfine couplings constants of the NMR active nuclei. Due to the compactness of the coordination sphere, the magnetic anisotropy of the paramagnetic center is small, and this makes the contact contribution to be the dominant one, even on the remote atoms. The sign of the hyperfine coupling constants and related spin densities is alternating on the nuclei of the ligand cycle, denoting a preponderant spin polarization mechanism. This is well reproduced by unrestricted DFT calculations. Those values are furthermore slightly decreasing in the actinide series, which indicates a small decrease of the covalency from  $U^{IV}$  to  $Pu^{IV}$ .

## INTRODUCTION

The paramagnetic properties of lanthanide +III (Ln<sup>III</sup>) complexes have been widely studied by NMR spectroscopy because of their applications in medicine, biology or magnetic resonance imaging<sup>1, 2, 3</sup> but also for the possibility to reach electronic and/or structural information on metallic complexes in solution.<sup>4,5</sup> The presence of a paramagnetic center induces an additional shift  $\delta_K^p$  on the NMR spectrum of nuclei  $K$  located on a ligand with respect to a diamagnetic analogue. This shift is decomposed in the sum of two terms as

$$\delta_K^p = \delta_K^{pc} + \delta_K^c \quad (1)$$

where  $\delta_K^c$  and  $\delta_K^{pc}$  are the Fermi contact and pseudocontact (dipolar) contributions, respectively. The Fermi contact shift  $\delta_K^c$  arises from the spin density at nucleus  $K$   $\rho^s(\mathbf{r}_K)$  as a consequence of spin delocalization and/or spin polarization. It might be expressed as :<sup>6</sup>

$$\delta_K^c = \frac{1}{N_A \mu_0 \mu_B g_e \gamma_K} \frac{A_K^c}{\hbar} \chi_m^s \quad (2)$$

where  $N_A$  is the Avogadro constant,  $\mu_0$  the magnetic permeability,  $\mu_B$  the Bohr magneton,  $g_e$  the free electron g-factor,  $\gamma_K$  the gyromagnetic ratio of the observed nucleus. The hyperfine coupling (HFC) constant  $A_K^c/\hbar$  depends on the spin density at the nuclear position and  $\chi_m^s$  is the spin contribution to the magnetic susceptibility. Usually, this equation is expressed in terms of  $\langle S_m \rangle$ , the thermal average of the electron spin magnetization.<sup>7,8</sup>  $\chi_m^s = N_A \mu_B g_e \langle S_m \rangle / B_0$  where  $B_0$  is the external field. The expression of  $\delta_K^c$  in terms of  $\langle S_m \rangle$  depends on  $B_0$  while Eq. 2 does not. For Ln<sup>III</sup> cations, the  $\langle S_m \rangle$  values can be considered to be independent on the ligands and were calculated first in 1972 by Golding and Halton<sup>9</sup>, then by Pinkerton *et al.*<sup>10</sup> in 1985 while we recently reported the  $\langle S_m \rangle$  values obtained from *ab initio* calculations for [Ln<sup>III</sup>(Et-DPA)<sub>3</sub>]<sup>3-</sup> complexes (Et-DPA: 4-ethyl-2,6-dipicolinic acid).<sup>11</sup> The  $\langle S_m \rangle$  values were calculated by Martel *et al.* using crystal field theory for An<sup>IV</sup> complexes to interpret the variation of <sup>17</sup>O NMR chemical shifts of actinide oxide compounds across the An<sup>IV</sup> series and from SO-CASPT2 for An<sup>III</sup> complexes.<sup>12</sup> It appeared that the  $\langle S_m \rangle$  values for actinide complexes do not follow those tabulated for Ln<sup>III</sup> cations, due to the larger interaction with the ligands leading to a splitting of the ground  $J$  manifold larger than thermal energy at room temperature. Consequently,  $\langle S_m \rangle$  and equivalently  $\chi_m^s$  must be evaluated for each complex.

Within the point-dipole approximation,<sup>13, 14</sup> the dipolar shift  $\delta_K^{pc}$  corresponds to the through-space magnetic dipolar interaction between the electronic magnetic moment of the paramagnetic center and the nuclear magnetic moment of the NMR-active nucleus  $K$  and can be expressed as, when the reference frame coincides with the principal directions of the magnetic susceptibility tensor  $\chi$ ,

$$\delta_K^{pc} = \frac{[\chi_{xx}(3x_K^2 - r_K^2) + \chi_{yy}(3y_K^2 - r_K^2) + \chi_{zz}(3z_K^2 - r_K^2)]}{12\pi N_A r_K^5} \quad (3)$$

where  $\chi_{xx}$ ,  $\chi_{yy}$  and  $\chi_{zz}$  are the three principal components of  $\chi$  and  $\mathbf{r}_K = (x_K, y_K, z_K)$  is the metal–nucleus vector.<sup>14</sup> When the symmetry is axial,  $\chi_{xx} = \chi_{yy}$  and Eq. 3 is then simplified as

$$\begin{aligned} \delta_K^{pc} &= \frac{[\chi_{xx}(3x_K^2 + 3y_K^2 - 2r_K^2) + \chi_{zz}(3z_K^2 - r_K^2)]}{12\pi N_A r_K^5} \\ &= \frac{[\chi_{xx}(-3z_K^2 + r_K^2) + \chi_{zz}(3z_K^2 - r_K^2)]}{12\pi N_A r_K^5} \\ &= \frac{[(\chi_{zz} - \chi_{xx})(3z_K^2 - r_K^2)]}{12\pi N_A r_K^5} \end{aligned}$$

And with  $z_K = r_K \cos \theta_K$ , one gets

$$\delta_K^{pc} = \frac{1}{12\pi N_A} \Delta\chi_{ax} \frac{3\cos^2\theta_K - 1}{r_K^3} \quad (4)$$

where  $\Delta\chi_{ax} = \chi_{\parallel} - \chi_{\perp} = \chi_{zz} - \frac{\chi_{xx} + \chi_{yy}}{2}$  describes the axial anisotropy of  $\chi$  and  $\theta_K$  is the polar angle. The last term  $G_K = \frac{3\cos^2\theta_K - 1}{r_K^3}$  is called the geometrical factor and characterizes the relative position of nucleus  $K$  to the paramagnetic cation.

Several methods were proposed to discriminate between the pseudocontact and Fermi contact contributions for  $\text{Ln}^{\text{III}}$  complexes,<sup>2, 5, 15</sup> based on Bleaney's theory.<sup>16</sup> The most successful methods are based on the dependence of the paramagnetic NMR (pNMR) chemical shifts with the lanthanide ion. They were developed considering the following assumptions: i) the states arising from the ground J-manifold are populated at room temperature, ii) the  $\text{Ln}^{\text{III}}$  complexes are isostructural across the series and the second order axial ligand-field parameter  $B_0^2$  and the HFC constant  $A_K^c/\hbar$  are constant along the  $\text{Ln}^{\text{III}}$  series, iii) the Fermi contact and pseudocontact shifts are proportional to the tabulated  $\langle S_m \rangle$  and Bleaney's parameters  $C_J$ ,<sup>10, 16, 17</sup> respectively. This model is based on the reminiscence of electronic structure of the  $\text{Ln}^{\text{III}}$  free ion in complexes due to the inner-shell behavior of the 4f orbitals, which are shielded from the ligands by the filled 5s5p orbitals. For actinide complexes, 5f orbitals are more available to covalent interaction with the ligands, due to their larger spatial extension as compared to the filled 6s6p and the splitting of the

free ion term by the ligands is larger than thermal energy at room temperature. Consequently, the assumption i) is no more valid for actinides. As shown in the isostructural  $[\text{Ln}^{\text{III}}(\text{DPA})_3]^{3-}$  series ( $\text{Ln} = \text{Ce} - \text{Yb}$ ) using CAS based methods,<sup>18</sup>  $B_0^2$  is decreasing along the series and many of the other crystal-field parameters are quantitative, which shows that the crystal-field parameter in Bleaney's equation must be thought as an effective parameter. In the early  $[\text{An}^{\text{IV}}(\text{DPA})_3]^{2-}$  series  $B_0^2$  is by far not constant, due to an important J mixing. For the same reasons, as already specified,  $\langle S_m \rangle$  and  $C_J$  tabulated for the lanthanides are not valid for the actinides. It makes Bleaney's theory even more inappropriate to model the Actinide Induced Shift (AIS) because of large crystal-field and spin-orbit interactions.

Alternative methods to separate the two contributions are based on the respective  $T^{-1}$  and  $T^{-2}$  temperature dependence of the Fermi contact and pseudocontact contributions.<sup>19,20</sup> Limiting the thermal expansion to those two terms has been criticized.<sup>21</sup> It has early been shown that a  $T^{-3}$  correction term can be necessary<sup>22</sup> and this was recently successfully applied in the  $[\text{Ln}^{\text{III}}(\text{DPA})_3]^{3-}$ ,  $[\text{An}^{\text{III}}(\text{DPA})_3]^{3-}$  and  $[\text{An}^{\text{VI}}\text{O}_2(\text{DPA})_2]^{2-}$ .<sup>11,23</sup>

The computation from first principles of pNMR shifts requires a balanced description of the multiconfigurational electronic structure of the paramagnetic center in order to describe its magnetic susceptibility, and, of the metal-ligand spin delocalization and polarization for the contact contribution. Many computational approaches to calculate pNMR shieldings are based on Kurland-McGarvey theory.<sup>24</sup> Firstly developed for a well separated Kramers doublet, the newest developments allow the inclusion of the zero-field splitting for systems with a larger degeneracy.<sup>25</sup> But those approaches are not suitable for lanthanide and actinide complexes, with many low-lying excited states magnetically coupled to the ground state and populated at room temperature. The description of those complexes by mean of a Spin Hamiltonian for the ground manifold is therefore not worth considering. The general case is described by the equation derived by Soncini and van den Heuvel.<sup>26</sup> Autschbach *et al.* evaluated the AIS in actinide tris-carbonate complexes and the methyl protons in  $(\text{C}_5\text{H}_5)_3\text{UCH}_3$  using the multi-configurational RASSCF method.<sup>27</sup> The magnetic properties of the paramagnetic center are correctly described by the active space comprising all the  $5f$  orbitals, and the spin polarization is rendered by considering the one-electron excitation on the top. But this strategy is neither easy, nor affordable in order to render the spin polarization until the most remote nuclei of the ligands.

When the hyperfine interaction reduces to its dipolar component, the Soncini equation leads to eq. 3, and further in axial cases to eq. 4. The computational approach focuses then on the *ab initio* evaluation of the anisotropy of the  $\chi$  tensor. This allows the full description of the paramagnetic center with all excited states, either partially populated or not, and strongly magnetically coupled.<sup>23</sup> We will follow this approach in this work. The Fermi contact term is better described using DFT in an unrestricted scheme. Studies of various  $\text{Gd}^{\text{III}}$  systems demonstrated that unrestricted SR-DFT (scalar relativistic density functional theory) based methods are able to accurately calculate the

hyperfine coupling of  $^{17}\text{O}$  nuclei directly bonded to a paramagnetic cation.<sup>28</sup> Similarly, the agreement between calculated and experimental  $^1\text{H}$  pNMR chemical shifts of  $\text{Ln}^{\text{III}}$  complexes with macrocyclic ligands was improved when Fermi contact shifts were included.<sup>29</sup>

The  $[\text{An}^{\text{IV}}(\text{DPA})_3]^{2-}$  complexes are isostructural across the  $\text{An}^{\text{IV}}$  series as revealed by SC-XRD experiments<sup>30</sup> and present an approximate  $D_3$  symmetry in solution with the axis of symmetry along the pseudo  $C_3$  axis. In this work,  $^1\text{H}$  and  $^{13}\text{C}$  AIS in  $[\text{An}^{\text{IV}}(\text{DPA})_3]^{2-}$  complexes are measured in  $[\text{D}_7]\text{DMF}$  solution and analyzed with the help of quantum chemistry calculations. The temperature variation of the AIS allows separating the Fermi contact and pseudocontact terms. This allows accessing experimental evaluation of the axial anisotropy of the susceptibility tensor, hyperfine coupling constants and spinning density at the NMR active nuclei. Those are compared to the *ab initio* values.

## EXPERIMENTAL AND COMPUTATIONAL SECTION

**Synthesis.**  $^{232}\text{Th}$ orium,  $^{238}\text{U}$ ranium,  $^{237}\text{Np}$ eptunium and  $^{239+240}\text{Pu}$ lunium are radioactive elements and have to be handled in dedicated facilities with appropriate equipment for radioactive materials. Their manipulation has been carried out at the ATALANTE facility (CEA-Marcoule, France). The experiments involving Np and Pu were performed in a regular air atmosphere negative pressure glove box with restrictive protocols, whereas Th and U were manipulated under fume hood.

2,6-dipicolinic acid ( $\text{H}_2\text{DPA}$ ) and tert-Butyl alcohol (t-BuOH) were obtained from Sigma-Aldrich.  $[\text{D}_6]\text{DMSO}$  and  $[\text{D}_7]\text{DMF}$  were purchased from Cortecnet or Eurisotop and used as received. Et – DPA ligand was synthesized in the lab according to the protocol described by Shelkov.<sup>31</sup> Et – DPA purity was checked by  $^1\text{H}$  NMR spectroscopy.  $^1\text{H}$  NMR (400 MHz,  $[\text{D}_6]\text{DMSO}$ ):  $\delta$  (ppm) 7.76 (s, 2H, H3), 2.65 (q,  $J = 7.58$  Hz, 2H, H5), 1.18 (t,  $J = 7.58$  Hz, 3H, H6). The hexachloride compounds of  $\text{An}^{\text{IV}}$ ,  $\text{Cs}_2\text{An}^{\text{IV}}\text{Cl}_6$ , were prepared according to a protocol described by Kooi *et al.*<sup>32</sup>

$\text{An}^{\text{IV}}$ -DPA/Et-DPA. All preparation and experiments were carried out under air. The  $\text{An}^{\text{IV}}$ -DPA/Et-DPA complexes were synthesized from a mixture of the solid precursor ( $\text{Cs}_2\text{An}^{\text{IV}}\text{Cl}_6$ ) and  $\text{Na}_2\text{DPA}$  /  $\text{Na}_2\text{Et} - \text{DPA}$  ligands in  $[\text{D}_7]\text{DMF}$  with a molar ratio  $\text{An}^{\text{IV}}/\text{DPA}$ ; Et-DPA of 1 / 8. The mixture was stirred for 15 min at room temperature and the ligand excess and the CsCl precipitates were removed by centrifugation. The resulting solution was isolated and set up for analysis.

**NMR spectroscopy.**  $^1\text{H}$  and  $^{13}\text{C}$  NMR spectra were recorded using 400 MHz Fourier transform spectrometer, Agilent DD2, set up for the study of radioactive samples.<sup>33</sup> Acquisitions and processing were performed with OpenVnmrJ 2.1 revA software (<https://openvnmrj.org/>). The spectra were collected at every 5 K step on the temperature range  $263\text{ K} < T < 333\text{ K}$ . Sample

temperature has been calibrated for the 5mm “OneProbe” with methanol and ethylene glycol (for low and high temperature respectively) sample tubes.

**Magnetic susceptibility measurements.** The molar magnetic susceptibilities  $\chi_m$  ( $\text{m}^3 \cdot \text{mol}^{-1}$ ) were determined from the chemical shift difference  $\Delta\delta$  between the  $^1\text{H}$  NMR signals of working and reference t-BuOH (tert-butyl alcohol) solutions using Evans method<sup>34</sup> on the temperature range 235-335 K according to

$$\chi_m^{exp} = \frac{3\Delta\delta}{10^3[\text{An}^{\text{IV}}]} \quad (5)$$

where  $\Delta\delta$  is dimensionless,  $[\text{An}^{\text{IV}}]$  is the molar concentration ( $\text{mol} \cdot \text{L}^{-1}$ ) of the paramagnetic element. Uncertainties values were estimated by taking into account  $\Delta\delta$  accuracies of NMR spectra and concentration measurements. The t – BuOH concentration used for these experiments was about  $0.1 \text{ mol} \cdot \text{L}^{-1}$ .  $\text{Pu}^{\text{IV}}$  and  $\text{Np}^{\text{IV}}$  concentrations were checked by alpha and gamma counting respectively.  $\text{Np}^{\text{IV}}$  and  $\text{U}^{\text{IV}}$  titrations were also performed by UV-vis spectrophotometry (after assay sample dilution in 1M HCl).

**Visible spectrophotometry.** The  $[\text{An}^{\text{IV}}(\text{DPA})_3]^{2-}$  complexes synthesized in  $[\text{D}_7]\text{DMF}$  solution were analyzed by visible absorption spectrophotometry using a Cary 5000 UV spectrophotometer (Agilent) between 400 and 800 nm. The  $\text{An}^{\text{IV}}(\text{DPA})_3(\text{C}_3\text{H}_5\text{N}_2) \cdot 3\text{H}_2\text{O}$  solid spectra were recorded using a Shimadzu UV-2600 spectrophotometer equipped with an integration sphere for reflection measurements. The  $\text{An}^{\text{IV}}(\text{DPA})_3(\text{C}_3\text{H}_5\text{N}_2) \cdot 3\text{H}_2\text{O}$  single crystals were ground to make a fine and homogeneous powder. The resulting powder were sealed with crystal tape and set up in the integration sphere.

**Wave-function theory calculations.** Two structures were considered: i) the  $[\text{An}^{\text{IV}}(\text{DPA})_3]^{2-}$  complexes ( $\text{An}=\text{U}$ ,  $\text{Np}$ ,  $\text{Pu}$ ) using the crystallographic  $\text{An}^{\text{IV}}(\text{DPA})_3(\text{C}_3\text{H}_5\text{N}_2)_2 \cdot 3\text{H}_2\text{O}$  structures (denoted XR);<sup>30</sup> ii) the symmetrized structure of the  $[\text{An}^{\text{IV}}(\text{Et-DPA})_3]^{2-}$  (denoted  $D_3$ ): the  $[\text{An}^{\text{IV}}(\text{DPA})_3]$  skeleton was symmetrized according to the  $D_3$  point group with Chemcraft software (<https://chemcraftprog.com/>). The ethyl group is added with three different angles from the aromatic ring,  $0^\circ$ ,  $45^\circ$  and  $90^\circ$  in order to represent the free rotation of the ethyl group.<sup>11</sup> For the first structures, the SO-CASPT2 results are taken from reference<sup>30</sup>. For the  $D_3$  structures, calculations were performed with the MOLCAS 7.8 suite of programs.<sup>35</sup> ANO-RCC basis sets were used: An TZP, O, N TZP, C DZP and H DZ. Firstly, SF-CASSCF (spin-free complete active space self consistent field) calculations<sup>36</sup> are performed with an active space composed of the seven  $5f$  orbitals of the metal and associated electrons, i.e. CAS(n,7). For  $\text{U}^{\text{IV}}$  21 triplets and 27 singlets are considered, for  $\text{Np}^{\text{IV}}$  35 quartets and 43 doublets, for  $\text{Pu}^{\text{IV}}$  35 quintets, 32 triplets and 17 singlets. Dynamical correlation is added using the CASPT2 (complete active space perturbation theory at 2nd order) method<sup>37</sup> with a level shift of 0.3 a.u. with state specific (SSCASPT2), state by state on top of CASSCF wave function. Scalar relativistic effects were taken into account by means of the Douglas-Kroll-Hess transformation,<sup>38</sup> and spin-orbit (SO) integrals were calculated

using the AMFI (Atomic Mean-Field Integrals) approximation.<sup>39</sup> Spin-orbit coupling (SOC) was included by a state interaction with the RASSI (restricted active space state interaction) method.<sup>40</sup> The calculations of magnetic properties were implemented in a local program. The magnetic susceptibilities were calculated according to the method of Vancoillie *et al.*<sup>41</sup> Crystal-field parameters were calculated with a local program written in Mathematica as described in references.<sup>42</sup>

**DFT calculations.** Mulliken spin population analyses were performed for the  $[\text{Ln}^{\text{III}}(\text{Et-DPA})_3]^{3-}$  and  $[\text{An}^{\text{IV}}(\text{Et-DPA})_3]^{2-}$  complexes using unrestricted DFT based methods with MOLCAS 7.8.<sup>35</sup> ANO-RCC-TZP basis sets were considered for all the atoms. Three functionals were compared: the hybrid PBE0,<sup>43</sup> the global hybrid M06 and M06-2X with respectively 27 and 54% HF exchange.<sup>44</sup> Calculations were performed using an unrestricted scheme with a fractional occupation of the seven  $5f$  orbitals. Those calculations do not take into account the spin-orbit coupling. The charge and spin distributions of the complex are better described by a fractional occupation than by one determinant. Effect of basis sets on the Mulliken populations are tested for the  $\text{U}^{\text{IV}}$  complex to complete the comparison (see Table SI-20) and the results are rather similar.

The isotropic hyperfine coupling constants were calculated with ORCA 4.0.1.2 suite of programs (ref=Neese, F. Software update: the ORCA program system, version 4.0 Wiley Interdisciplinary Reviews: Computational Molecular Science 2018, 8 e1327). Scalar relativistic effects were taken into account with ZORA Hamiltonian and SOC effects were introduced perturbatively. The ‘resolution of identity’ RIJCOSX approximation was used for the formation of the Coulomb and exchange-type matrices (ref= Neese, F. An improvement of the resolution of the identity approximation for the formation of the Coulomb matrix J. Comput. Chem. 2003 24 1740-1747). The HFC constants were calculated with unrestricted DFT method using PBE0 functional. SARC-ZORA-TZVP basis set was used for An atoms with SARC/J auxiliary basis set (ref=Pantazis, D. A., Neese, F. All-electron scalar relativistic basis sets for the actinides J. Chem. Theory Comput. 2011 7 677-684). For a better description of spin population near the nuclei, IGLO-II basis set was used for the C atoms (ref=Kutzelnigg, W. Fleischer, U. Schindler M. Deuterium and shift calculation Springer 1990 pp 165-262), and for the rest of the atoms, TZVP basis sets were used with the auxiliary basis sets using AUTOAUX (ref=Stroychev, G. L.; Auer, A. A. ; Neese, F. Automatic generation of auxiliary basis sets J. Chem. Theory Comput. 2017 13 554-562) feature in ORCA.

## RESULTS AND DISCUSSION

**Spectrophotometric experiments.** Visible absorption spectra were obtained on  $\text{An}^{\text{IV}}(\text{DPA})_3(\text{C}_3\text{H}_5\text{N}_2)_2 \cdot 3\text{H}_2\text{O}$  solid compounds previously studied by SC-XRD.<sup>30</sup> The absorption spectra of  $\text{An}^{\text{IV}}$  cations result from  $f$ - $f$  transitions that are very sensitive to the coordination sphere (symmetry and ligand’s features) providing a specific signature of each



complex. The mirror patterns observed in Figure 1 between solid state and solution spectra (in reflectance and absorption respectively) confirm the stability of the  $[\text{An}^{\text{IV}}(\text{DPA})_3]^{2-}$  complexes in  $[\text{D}_7]\text{DMF}$  solution.

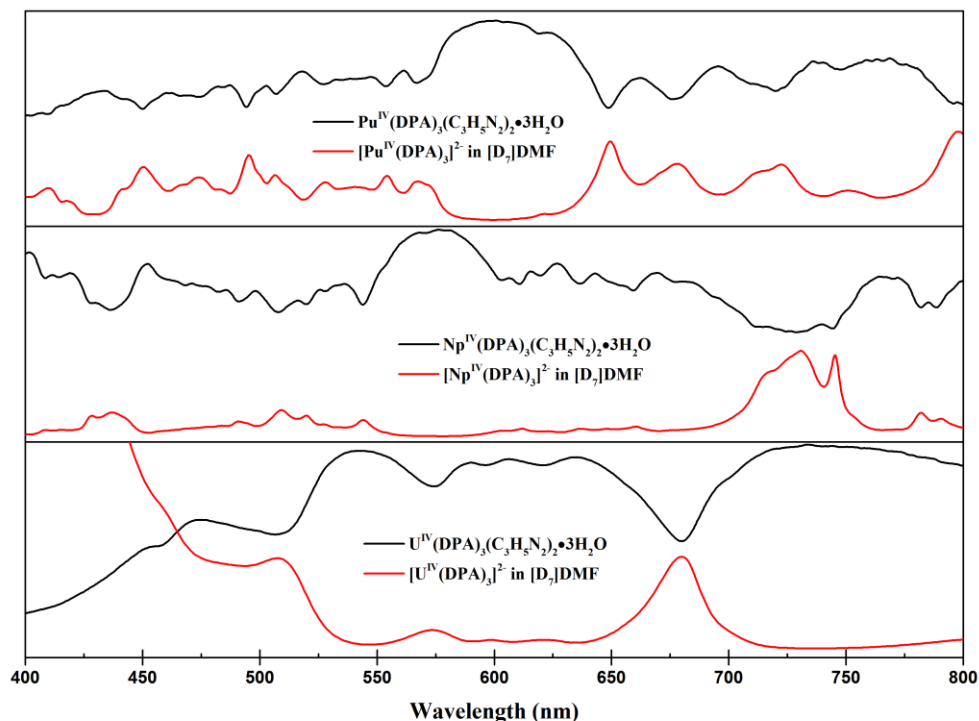


Figure 1: Visible reflectance spectra on  $\text{An}^{\text{IV}}(\text{DPA})_3(\text{C}_3\text{H}_5\text{N}_2)_2 \cdot 3\text{H}_2\text{O}$  crystals (black) and visible absorption spectra of  $[\text{An}^{\text{IV}}(\text{DPA})_3]^{2-}$  complexes dissolved in  $[\text{D}_7]\text{DMF}$  solution (red).

### Molar magnetic susceptibility

The magnetic susceptibility  $\chi_m$  as deduced (Figure 2) by Evans method<sup>34</sup> for the  $[\text{An}^{\text{IV}}(\text{DPA})_3]^{2-}$  complexes in  $[\text{D}_7]\text{DMF}$  solution at 298 K is given in Table 1. For the comparison with SO-CASPT2, we first considered the  $\text{An}^{\text{IV}}(\text{DPA})_3(\text{C}_3\text{H}_5\text{N}_2)_2 \cdot 3\text{H}_2\text{O}$  solid compounds, where the complex is not strictly axial, due the presence of the counter-ions. The  $\chi$  tensor completely deviates from the axial symmetry, both in directions and values axis (see Figure SI-5 and Table SI-13). The dipolar contributions to the AIS calculated according to Eq. 3 are given in Table SI-2. Since none of the principal axes of the  $\chi$  tensor is along the pseudo  $C_3$  axis, the shifts for chemically equivalent atoms completely differ, which is not in accordance with the experimental spectra. One expects the complex to be symmetrical in solution. To be consistent with experimental NMR data, the X-ray structures were symmetrized according to  $D_3$  point group (Table SI-21) with Chemcraft software.

The magnetic susceptibility tensors  $\chi$  calculated with SO-CASPT2 on the  $D_3$   $[\text{An}^{\text{IV}}(\text{DPA})_3]^{2-}$  complexes are given in Table 1 and compared to the experimental  $\chi_m$  values deduced for  $[\text{An}^{\text{IV}}(\text{DPA})_3]^{2-}$  complexes in  $[\text{D}_7]\text{DMF}$  solution by Evans method in Figure 2. Due to the axial symmetry, it reduces to its  $\chi_{\parallel}$  and  $\chi_{\perp}$  components. The isotropic average and the anisotropy are deduced as  $\chi_m = \frac{1}{3}(\chi_{\parallel} + 2\chi_{\perp})$  and  $\Delta\chi_{ax} = \chi_{\parallel} - \chi_{\perp}$ , respectively. The isotropic magnetic susceptibilities  $\chi_m$  calculated with SO-CASPT2 at 298 K are in rather good agreement with the experimental values. The three  $\chi_i$  values are rather similar and the anisotropy small because of the compactness of the coordination sphere and the symmetric stacking of O and N donor atoms (3O, 3N, 3O) along the Z axis in a tricapped trigonal prismatic environment. It follows that the principal axes frame of the  $\chi$  tensor is very sensitive to distortions. This shows that there is a symmetrization of the structure in solution and in the following, we will only provide the results obtained on the  $D_3$  structures (Table SI-21).

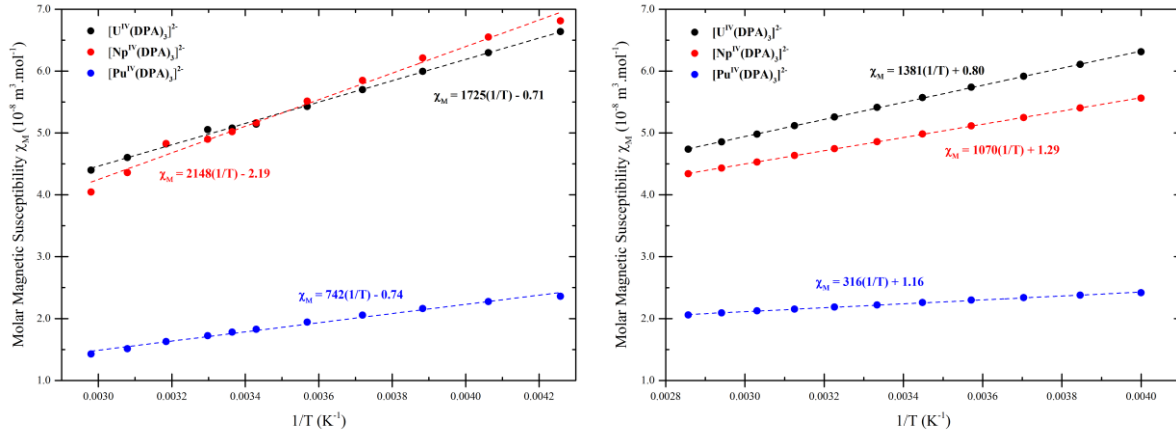


Figure 2: Experimental (left) and SO-CASPT2 (right) molar magnetic susceptibilities of  $[\text{An}^{\text{IV}}(\text{DPA})_3]^{2-}$  complexes vs the reverse of temperature,  $1/T$  ( $\text{K}^{-1}$ ). The linear regressions are represented in dashed lines.

## Electronic structure

The energies of the  $[\text{An}^{\text{IV}}(\text{DPA})_3]^{2-}$  complexes in the  $D_3$  structure are given in Table SI-11. The active  $5f$  orbitals are shown in Figure 3. The lowest one, of symmetry  $a_2$ , is non-bonding, then there is a group of three orbitals ( $e \oplus a_2$ ) denoting a  $\pi$  anti-bonding character with the O atoms, and finally, the three last ones ( $a_1 \oplus e$ ) with a  $\sigma$  anti-bonding character with the ligands. The energy levels, their natures and also the trends of the crystal-field parameters of the  $\text{An}^{\text{IV}}(\text{DPA})_3(\text{C}_3\text{H}_5\text{N}_2)_2 \cdot 3\text{H}_2\text{O}$  series ( $\text{An}^{\text{IV}} = \text{U}, \text{Np}$  and  $\text{Pu}$ ) were discussed.<sup>30</sup> The ground  $LS$  terms for  $\text{U}^{\text{IV}}$ ,  $\text{Np}^{\text{IV}}$  and  $\text{Pu}^{\text{IV}}$  ions are  $^3H$ ,  $^4I$  and  $^5I$  respectively and are split due to the presence of the ligands from  $2500 \text{ cm}^{-1}$  for  $\text{U}^{\text{IV}}$  to  $4000 \text{ cm}^{-1}$  for  $\text{Pu}^{\text{IV}}$  in the CASPT2 calculations. The SO states arising from the respective ground J terms are split around  $1100\text{-}1500 \text{ cm}^{-1}$ , quite larger than in the  $[\text{Ln}^{\text{III}}(\text{DPA})_3]^{3-}$  complexes where the splitting is around  $300 \text{ cm}^{-1}$ , since the  $5f$  orbitals interact more with the ligands than the  $4f$  ones in lanthanides.

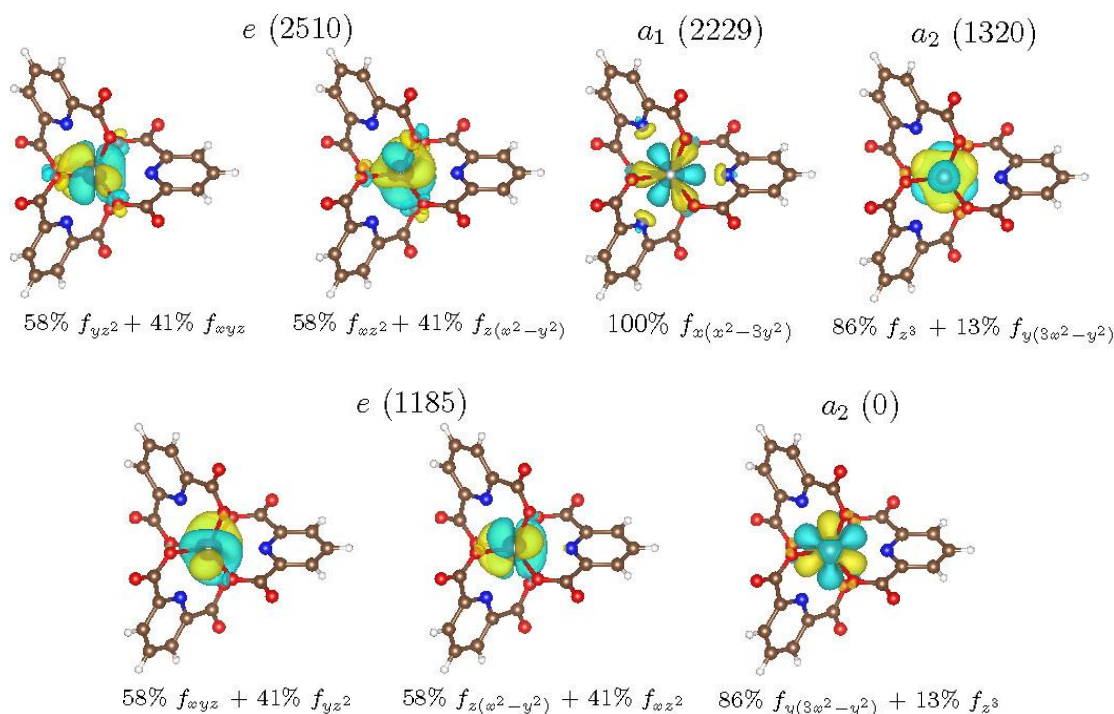


Figure 3: Canonical 5f active orbitals of the  $[\text{Np}^{\text{IV}}(\text{DPA})_3]^{2-}$  complex in  $D_3$  symmetry. The canonical energies are given in parenthesis. The isosurface value is  $0.14 \text{ e}^- \text{bohr}^{-3}$ .

In the  $\text{U}^{\text{IV}}$  complex, the ground state is non-degenerate and therefore, non-magnetic. In this case, the excited states play a key role to the susceptibility, on one hand by coupling with the excited states and on the other hand, when low-lying, being populated at room temperature. In the  $\text{U}^{\text{IV}}$  complex, a triplet (163, 169 and  $171 \text{ cm}^{-1}$ ) and a doublet (246 and  $269 \text{ cm}^{-1}$ ) are low-lying and populated at room temperature. In the  $\text{Pu}^{\text{IV}}$  complex, the ground state is a non-Kramers doublet (with a gap of  $0.4 \text{ cm}^{-1}$ ) and there is partially populated triplet (399, 407,  $450 \text{ cm}^{-1}$ ) states. The lower SO states for the Kramers  $\text{Np}^{\text{IV}}$  complex are a symmetrical Kramers doublet, KD1 with g-values: 2.57, 2.69, 2.19 and a thermally populated low lying excited doublet, KD2 at  $68 \text{ cm}^{-1}$  with g-values: 0.04, 0.002, 3.90. Contributions from the ground LS manifolds to these SO states are around 85-88 % and notably, the most important J mixing is observed with the excited  $^1G$  (10-11%) for  $\text{U}^{\text{IV}}$ ,  $^2H$  (12-13%) for  $\text{Np}^{\text{IV}}$  and  $^3D$  (9-10%) for  $\text{Pu}^{\text{IV}}$  manifolds. As the splitting of the ground J manifolds of these  $\text{An}^{\text{IV}}$  complexes is larger than the room temperature energy, the thermal populations in the low lying SO states will change with temperature translating a complex temperature dependency of the magnetic properties.

Table 1: Magnetic susceptibility  $\chi$  and spin-only magnetic susceptibility  $\chi^S$  tensors ( $10^{-8} \text{ m}^3 \cdot \text{mol}^{-1}$ ) at 298 K for the  $[\text{An}^{\text{IV}}(\text{DPA})_3]^{2-}$  complexes from SO-CASPT2 and for the  $[\text{Yb}^{\text{III}}(\text{DPA})_3]^{3-}$  complexes from SO-CASSCF using the  $D_3$  structures.

	$\chi_m^{\text{exp}}$	$\chi_{\perp}^{\text{cal}}$	$\chi_{\parallel}^{\text{cal}}$	$\Delta\chi_{\text{ax}}^{\text{cal}}$	$\chi_m^{\text{cal}}$	$\chi_{\perp}^{\text{S,cal}}$	$\chi_{\parallel}^{\text{S,cal}}$	$\Delta\chi_{\text{ax}}^{\text{S,cal}}$	$\chi_m^{\text{S,cal}}$
$\text{U}^{\text{IV}}$	5.1 ( $\pm 0.1$ )	5.15	6.03	0.88	5.44	-1.19	-1.33	-0.14	-1.24
$\text{Np}^{\text{IV}}$	5.0 ( $\pm 0.3$ )	4.48	5.70	1.22	4.89	-1.60	-2.03	-0.43	-1.74
$\text{Pu}^{\text{IV}}$	1.8 ( $\pm 0.2$ )	2.30	2.09	-0.21	2.23	-1.36	-1.73	-0.37	-1.48
$\text{Yb}^{\text{III}}$		11.57	8.78	-2.79	10.64	1.46	1.11	-0.35	1.34

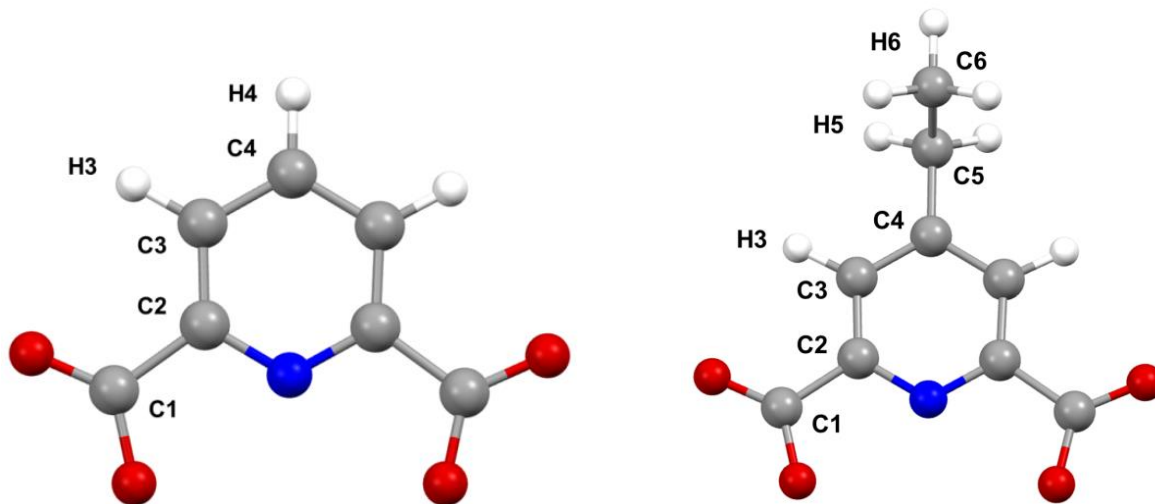


Figure 4:  $\text{DPA}^{2-}$  (left) and  $\text{Et-DPA}^{2-}$  (right) molecules with the numbering of the  $^1\text{H}$  and  $^{13}\text{C}$  nuclei.

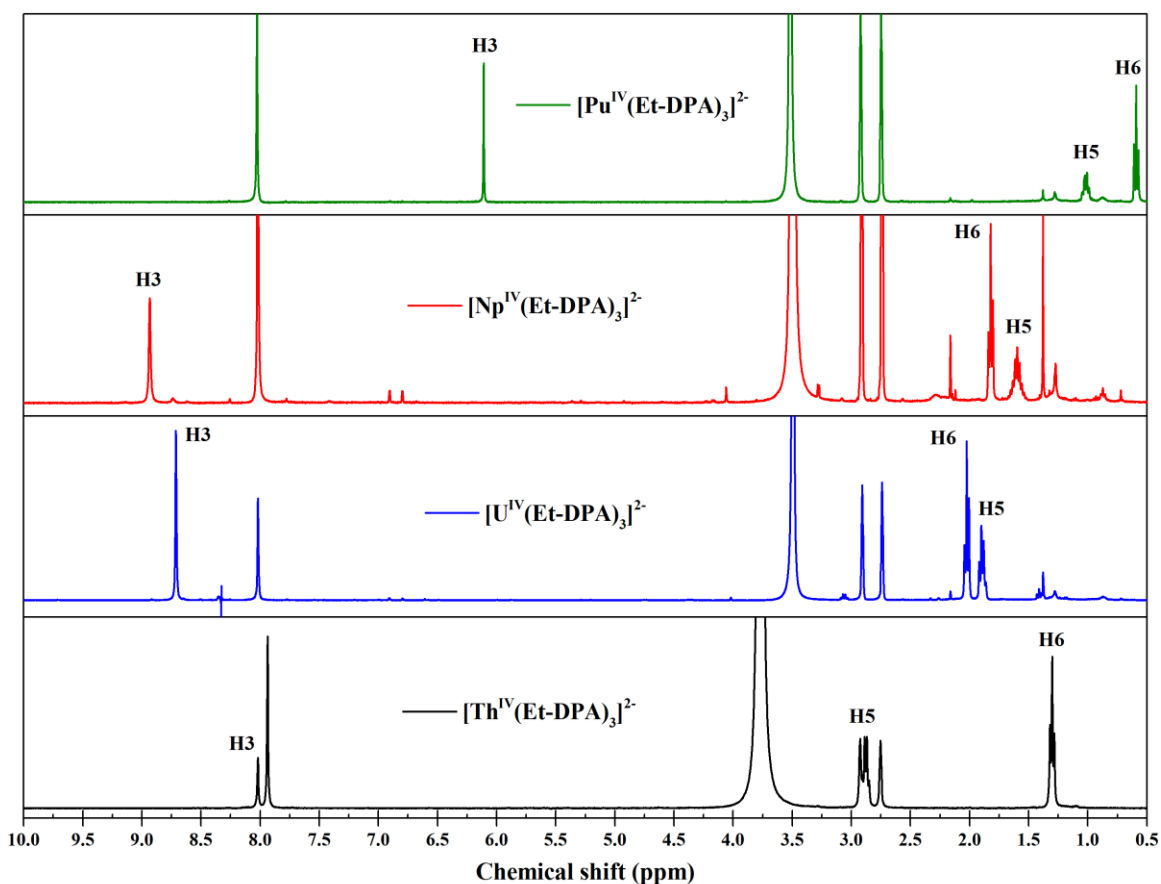


Figure 5:  $^1\text{H}$  NMR spectra of  $[\text{An}^{\text{IV}}(\text{Et-DPA})_3]^{2-}$  complexes in  $[\text{D}_7]\text{DMF}$  solution at 9.4 T and 298 K.

### Analysis of the AIS.

Both  $[\text{An}^{\text{IV}}(\text{DPA})_3]^{2-}$  and  $[\text{An}^{\text{IV}}(\text{Et-DPA})_3]^{2-}$  complexes were studied by NMR spectroscopy as the later provides supplementary  $^1\text{H}$  and  $^{13}\text{C}$  nuclei further from the paramagnetic center. The  $^1\text{H}$  and  $^{13}\text{C}$  nuclei of the DPA and Et-DPA molecules are numbered according to Figure 4.  $^1\text{H}$  NMR spectra of  $\text{An}^{\text{IV}} - \text{DPA}/\text{Et} - \text{DPA}$  complexes were recorded in  $[\text{D}_7]\text{DMF}$  at 298 K. Figure 5 shows the  $^1\text{H}$  spectra of  $[\text{An}^{\text{IV}}(\text{Et-DPA})_3]^{2-}$  complexes as example. The  $^{13}\text{C}$  NMR spectra of  $[\text{An}^{\text{IV}}(\text{Et-DPA})_3]^{2-}$  complexes recorded in  $[\text{D}_7]\text{DMF}$  at 298 K are reported in Figures SI-1. The peaks assignment were performed from gHMBC and gHSQC NMR experiments (gHSQC and gHMBC are 2-dimensional inverse  $^1\text{H}$ ,  $^{13}\text{C}$  correlation techniques that allow for the determination of carbon to hydrogen atoms connectivity: The former is selective for direct C-H coupling while the latter gives longer range couplings: 2 to 3 bonds). The 2D spectra are displayed in Figures SI-1 for  $\text{An}^{\text{IV}}$  complexes with both DPA ligands and all observed chemical shifts collected within 90K temperature range reported in Tables SI-1. The paramagnetic contributions to the chemical shifts

were deduced by using  $[\text{Th}^{\text{IV}}(\text{DPA})_3]^{2-}$  and  $[\text{Th}^{\text{IV}}(\text{Et-DPA})_3]^{2-}$  as diamagnetic references.  $^1\text{H}$  and  $^{13}\text{C}$  chemical shifts and the AIS obtained at room temperature (298 K) are reported in Table 2.

Table 2: Chemical shifts  $\delta_K$ , paramagnetic induced shifts  $\delta_K^p$ , pseudocontact  $\delta_K^{pc}$  and Fermi contact  $\delta_K^c$  contributions (ppm) of  $^{13}\text{C}$  and  $^1\text{H}$  nuclei in  $[\text{An}^{\text{IV}}(\text{Et-DPA})_3]^{2-}$  complexes in  $[\text{D}_7]\text{DMF}$  solution at 9.4 T and 298 K.  $\delta_K^{pc}$  are deduced from the fitting of the AIS temperature dependence according to eq. 9 and  $\delta_K^c$  as  $\delta_K^c = \delta_K^p - \delta_K^{pc}$ . Values from  $[\text{Yb}^{\text{III}}(\text{Et-DPA})_3]^{3-}$  complex are given for comparison.<sup>11</sup> %pc gives the weight of the dipolar contribution.

		C1	C2	C3	C4 <sup>A</sup>	C5	C6	H3 <sup>A</sup>	H4	H5	H6
$\text{Th}^{\text{IV}}$	$\delta_K$	171.51	151.61	124.96	141.4/159.2 <sup>a</sup>	28.35	13.89	8.07/7.95	8.249	2.89	1.31
$\text{U}^{\text{IV}}$	$\delta_K$	113.29	147.28	153.54	136.9/155.6	35.34	8.76	8.68/8.72	12.947	1.9	2.04
	$\delta_K^p$	-58.22	-4.33	28.58	-4.57/-3.61	6.99	-5.13	0.60/0.77	4.698	-0.99	0.73
	$\delta_K^{pc}$	-0.85	-9.88	-4.09	-3.36/-3.36	-1.56	-1.10	-2.27/-2.27	-2.05	-1.25	-0.97
	$\delta_K^c$	-57.4	5.6	32.7	-1.2/-0.3	8.6	-4.0	2.9/3.0	6.7	0.3	1.7
	%pc	1%	64%	11%	74% / 93%	15%	22%	44%/43%	23%	83%	36%
$\text{Np}^{\text{IV}}$	$\delta_K$	97.45	156.93	160.86	159.2/152.0	34.51	8.69	9.10/8.94	11.969	1.61	1.83
	$\delta_K^p$	-74.1	5.3	35.9	17.77/-7.2	6.2	-5.2	1.03/1.0	3.72	-1.3	0.5
	$\delta_K^{pc}$	-2.37	-35.23	-14.55	-11.96/-11.96	-5.54	-3.91	-8.03/-8.03	-7.28	-4.43	-3.44
	$\delta_K^c$	-71.7	40.6	50.5	29.7/4.8	11.7	-1.3	9.1 / 9.0	11.0	3.2	4.0
	%pc	3%	46%	22%	29% / 72%	32%	75%	47%/47%	40%	58%	46%
$\text{Pu}^{\text{IV}}$	$\delta_K$	144.55	150.11	139.38	133.2/151.1	34.29	10.44	6.28/6.11	8.104	1.01	0.59
	$\delta_K^p$	-26.96	-1.5	14.42	-9.24/-8.1	5.94	-3.45	-1.79/-1.84	-0.145	-1.88	-0.72
	$\delta_K^{pc}$	0.62	9.64	3.97	3.26/3.26	1.51	1.06	2.19/2.19	1.98	1.20	0.93
	$\delta_K^c$	-27.6	-11.1	10.4	-12.5/-11.3	4.4	-4.5	-4.0/-4.0	-2.1	-3.1	-1.7
	%pc	2%	46%	28%	21% / 22%	25%	19%	35% / 35%	48%	28%	36%
$\text{Yb}^{\text{III}}$	$\delta_K$	-15.968	-28.686	-15.102	- / -4.991	-3.924	-2.225	- / -4.727	-	-2.759	-2.084
	$\delta_K^{pc}$ <sup>B</sup>	-0.22	-22.94	-9.40	- / -7.76	-3.62	-2.63	- / -5.10	-	-3.01	-2.36
	$\delta_K^c$	-15.7	-5.8	-5.7	- / 2.8	-0.3	0.4	- / 0.4	-	0.3	0.3
	%pc	1%	80%	62%	- / 74%	93%	87%	- / 93%	-	93%	90%

<sup>A</sup>:  $[\text{An}^{\text{IV}}(\text{DPA})_3]^{2-} / [\text{An}^{\text{IV}}(\text{Et-DPA})_3]^{2-}$ ; <sup>B</sup>:  $\delta_K$  and geometrical factors  $G_K$  are drawn from <sup>11</sup>

In the case of no Fermi contact contribution, the ratio between the pNMR shifts of two nuclei  $K$  and  $K'$  simplifies to the ratio of the geometrical factors

$$R_{K,K'} = \frac{\delta_K^p}{\delta_{K'}^p} = \frac{\delta_K^{pc}}{\delta_{K'}^{pc}} = \frac{G_K}{G_{K'}} \quad (6)$$

The  $R_{K,K'}$  values calculated from the ratio of the geometrical parameters and of the  $^1\text{H}$  AIS are given in Table 3. The strong deviation between  $R_{K,K'}$  values calculated from  $D_3$  symmetrized X-ray structures and experimental  $^1\text{H}$  AIS cannot be explained by structural variations between solid-state and solution but only by the presence of a non-negligible Fermi contact term. This shows that

the AIS can not be reduced to the dipolar contributions. This was the case for the early  $[\text{Ln}^{\text{III}}(\text{Et-DPA})_3]^{3-}$  complexes ( $\text{Ln}^{\text{III}}=\text{Ce}^{\text{III}} - \text{Eu}^{\text{III}}$ ) particularly with  $\text{Nd}^{\text{III}}$  and  $\text{Eu}^{\text{III}}$  cations and  $[\text{An}^{\text{III}}(\text{Et-DPA})_3]^{3-}$  complexes while a very good agreement was observed for the second part of the  $\text{Ln}^{\text{III}}$  series ( $\text{Ln}^{\text{III}}=\text{Tb}^{\text{III}} - \text{Yb}^{\text{III}}$ ).<sup>11</sup>

Table 3:  $R_{K,K'}$  (see Eq. 6) from the geometrical factors and the AIS for the  $^1\text{H}$  nuclei in  $[\text{An}^{\text{IV}}(\text{DPA})_2]^{2-}$ ,  $[\text{An}^{\text{IV}}(\text{Et-DPA})_2]^{2-}$  ( $D_3$  geometries) and  $[\text{Ln}^{\text{III}}(\text{Et-DPA})_2]^{3-}$  complexes at 9.4 T and 298 K.

	$\frac{G_{H3}}{G_{H4}}$	$\frac{\delta_{H3}^p}{\delta_{H4}^p}$	$\frac{G_{H3}}{G_{H6}}$	$\frac{\delta_{H3}^p}{\delta_{H6}^p}$	$\frac{G_{H5}}{G_{H6}}$	$\frac{\delta_{H5}^p}{\delta_{H6}^p}$
$\text{U}^{\text{IV}}$	1.11	0.12	2.33	1.05	1.29	-1.36
$\text{Np}^{\text{IV}}$	1.10	0.27	2.33	1.90	1.29	-2.46
$\text{Pu}^{\text{IV}}$	1.10	Inf.	2.34	2.56	1.29	2.61
$\text{Yb}^{\text{III}}$ <sup>a</sup>	/	/	2.16	$2.15 \pm 0.2$	1.27	$1.4 \pm 0.1$

<sup>a</sup> from ref <sup>11</sup>

For  $\text{Ln}^{\text{III}}$  complexes, the separation of Fermi contact and pseudocontact contributions can be performed from a temperature variation analysis.<sup>19, 20, 45</sup> Eqs. 1 to 4 give

$$\delta_K^p = \frac{1}{\mu_0 \mu_B g_e \gamma_K N_A} \frac{A_K^c}{\hbar} \chi_m^S + \frac{1}{12\pi N_A} G_K \Delta \chi_{ax} \quad (7)$$

Assuming  $T^{-1}$  and  $T^{-2}$  variations for the Fermi contact and pseudocontact terms respectively,  $\chi_m^S = \chi_m^{S'}/T$  and  $\Delta \chi_{ax} = \Delta \chi_{ax}'/T^2$ , Eq. 7 becomes

$$\delta_K^p = \frac{1}{\mu_0 \mu_B g_e \gamma_K N_A} \frac{A_K^c}{\hbar} \frac{\chi_m^{S'}}{T} + \frac{1}{12\pi N_A} G_K \frac{\Delta \chi_{ax}'}{T^2} = \frac{\alpha_K^c}{T} + \frac{\alpha_K^{pc}}{T^2} \quad (8)$$

Consequently, the linear regression of  $\delta_K^p T = f(1/T)$  curves allows evaluating the two contributions, the slope and the intercept leading to the pseudocontact and Fermi contact terms, respectively.  $^1\text{H}$  NMR spectra of  $[\text{An}^{\text{IV}}(\text{DPA})_3]^{2-}$  and  $[\text{An}^{\text{IV}}(\text{Et-DPA})_3]^{2-}$  complexes and  $^{13}\text{C}$  NMR spectra of  $[\text{An}^{\text{IV}}(\text{Et-DPA})_3]^{2-}$  were recorded in the temperature range 263 – 333 K and corrected from the diamagnetic  $\text{Th}^{\text{IV}}$  reference as shown in Figure 6 for the  $\text{Np}^{\text{IV}}$  complex as an example (See Figure SI-2 and 3 for  $\text{U}^{\text{IV}}$  and  $\text{Pu}^{\text{IV}}$  complexes). The results for the fit by Eq. 8 are summarized in Tables SI-4 and SI-6. The coefficient of determination  $R^2$  is small for some atoms. Furthermore, in Eq. 8,  $\alpha_K^{pc}$  is proportional to  $G_K$ ,  $\alpha_K^{pc} = G_K \beta^{pc}$  where  $\beta^{pc}$  is independent of the NMR active nucleus  $K$ . The ratio of two  $\alpha_K^{pc}$  should equal the ratio of two corresponding geometrical factors  $G_K$ , but according to Tables SI-5 and 7, it is clearly not the case, showing that Eq. 8 is not valid in the present case.

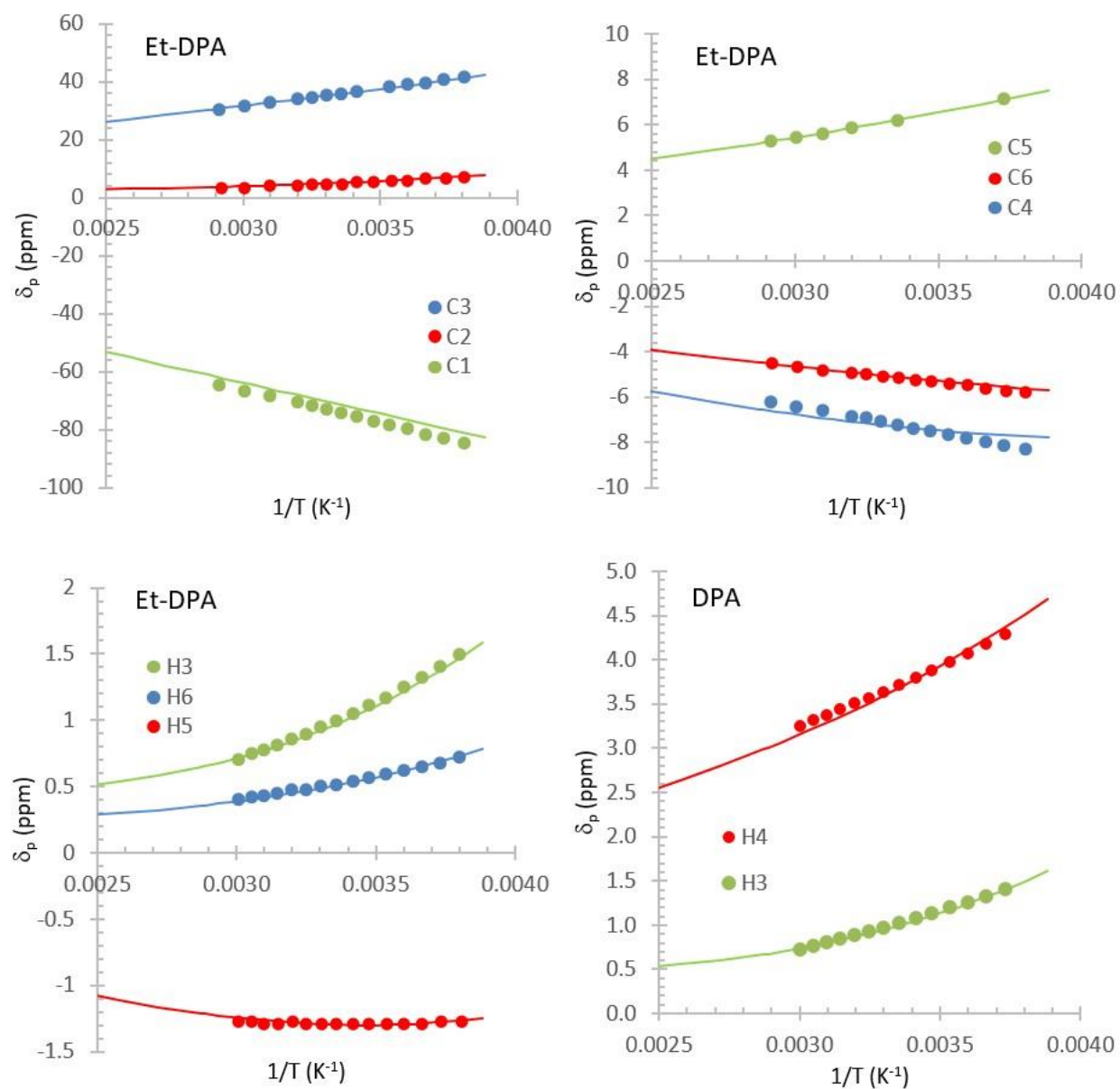


Figure 6:  $^{13}C$  (up) and  $^1H$  (down) AIS (ppm) in  $[Np^{IV}(Et-DPA)_3]^{2-}$  and  $[Np^{IV}(DPA)_3]^{2-}$  ( $^1H$  nuclei only) complexes vs the reverse of temperature ( $K^{-1}$ ) at 9.4 T. The fit by Eq. 9 is represented in solid lines. See Figure SI-2 and 3 for  $U^{IV}$  and  $Pu^{IV}$  cases respectively.

The fit of the AIS temperature dependence can be improved by re-considering orders in the temperature expansion of  $\delta_K^c$  and  $\delta_K^{pc}$ . Indeed, the temperature dependence of the *ab initio* magnetic susceptibility anisotropies  $\Delta\chi_{ax}$  denote a significant amount of  $T^{-1}$  (from 44 to 66% depending on the metallic cation, see Table SI-9) compared to  $T^{-2}$  and  $T^{-3}$  terms. Regarding the



contact contribution, the temperature dependence of the *ab initio*  $\chi_m^S$  is clearly dominated by the  $T^{-1}$  contribution (82, 87 and 92% for  $U^{IV}$ ,  $Np^{IV}$  and  $Pu^{IV}$  respectively, see Table SI-8). Consequently,  $\Delta\chi_{ax}$  should be described by its  $T^{-1}$ ,  $T^{-2}$  and  $T^{-3}$  contributions, while for  $\chi_m^S$ , the  $T^{-1}$  term is sufficient. Eq. 8 becomes accordingly

$$\delta_K^p = \frac{1}{\mu_0 \mu_B g_e N_A} \frac{1}{\gamma_K} \frac{A_K}{\hbar} \frac{\chi_m^{S'}}{T} + \frac{1}{12\pi N_A} G_K \frac{\Delta\chi'_{ax}}{T} \left(1 + \frac{\tau_1}{T} + \frac{\tau_2}{T^2}\right) \quad (9)$$

The  $T^{-1}$  term appears now in both, the contact and the dipolar terms. It means that Eq. 9 is not able to unravel those contributions, without further information. In order to overcome this point, the values of  $\tau_1$  and  $\tau_2$  are taken from the fitting of the SO-CASPT2  $\Delta\chi_{ax}$  temperature dependence. They are given by the ratios  $\frac{b}{a}$  and  $\frac{c}{a}$  respectively from Table SI-9 and reported Table 4. Similarly,  $\chi_m^{S'}$  is a multiplication factor to the contact contribution, and cannot be optimized by a fitting procedure. The SO-CASPT2 value as given in Table 1 is therefore considered. The values of  $\frac{A_K}{\hbar}$  and  $\Delta\chi'_{ax}$  are optimized to fit the AIS for all NMR-active nuclei at all available temperatures, by a root mean square procedure. The fitted parameters are given in Table 4 and SI-10. We reached an excellent fit as confirmed by the smallness of the agreement factor (AF) (see Figures 6, SI-2 and SI-3).

Table 4: Fitting parameters  $\Delta\chi'_{ax}$  ( $10^{-6} \text{ m}^3 \cdot \text{K}^3 / \text{mol}$ ) of eq. 9 from  $^1\text{H}$  and  $^{13}\text{C}$  AIS in  $[\text{An}^{IV}(\text{Et-DPA})_3]^{2-}$  and  $[\text{An}^{IV}(\text{DPA})_3]^{2-}$  complexes with  $\text{An}^{IV} = U^{IV}$ ,  $Np^{IV}$  and  $Pu^{IV}$  at 9.4 T.  $\tau_1$  and  $\tau_2$  are taken from SO-CASPT2, Table SI-9.  $\Delta\chi_{ax}$  ( $10^{-8} \text{ m}^3 \cdot \text{mol}^{-1}$ ) is given at 298 K.  $\chi_{\perp} = \chi_m^{exp} - \Delta\chi_{ax}/3$  and  $\chi_{\parallel} = \Delta\chi_{ax} + \chi_{\perp}$  with  $\chi_m^{exp}$  taken from Table 1.

	$\Delta\chi'_{ax}$	$\tau_1$	$\tau_2$	AF <sup>a</sup>	$\Delta\chi_{ax}$	$\chi_{\perp}$	$\chi_{\parallel}$
$U^{IV}$	3.10	94(±3)	-20301(±402)	0.9 %	1.13	4.72	5.85
$Np^{IV}$	9.51	232(±7)	-48182(±1021)	0.7 %	3.95	3.68	7.63
$Pu^{IV}$	-2.28	-295(±1)	11572(±247)	2.4 %	-1.07	2.16	1.09

<sup>a</sup>  $AF = [\sum_K (\delta_K^p - \delta_K^p(fit))^2 / \sum_K (\delta_K^p)^2]^{\frac{1}{2}}$

The dipolar and Fermi contact shifts are evaluated from Eq. 9 and are reported in Table 2 at 298 K. The dipolar contribution is dominant in the  $\text{Yb}^{III}$  complex, except for C1, where the geometrical factor vanishes due its angle relative to the  $C_3$  axis. This weight increases with the distance to the paramagnetic site, due to the vanishing of the contact contribution. On the contrary, for the actinide complexes, the contact is usually dominant, except for some C4 ( $U^{IV}$  case) and remote  $^1\text{H}$  (H5). The weight of the dipolar contribution is smaller in the actinide complexes, both because the dipolar contribution is smaller and the contact one larger. The susceptibility is smaller in the actinide complexes as shown in Table 1, the orbital and spin contributions being opposite, following third Hund's rule and the contact larger, especially on the carbons, likely due to the larger covalent interaction of the  $5f$  with the ligands. The value of the  $\Delta\chi_{ax}$  deduced from the fitting procedure as given in Table 4 are in good agreement with the SO-CASPT2 values given in Table

1.  $\Delta\chi_{ax}$  changes of sign between  $U^{IV}$ ,  $Np^{IV}$  and  $Pu^{IV}$ , in accordance with the change of sign of the  $\langle J||\alpha||J \rangle$  reduced matrix element of crystal field theory.<sup>46</sup>

The different contributions to the AIS are represented in Figure 7. The geometrical parameter is large for atoms close from the paramagnetic center and in the equatorial plane: it is the largest for C2 and the smallest for C1, which lies almost at the angle where  $3\cos^2\theta_K - 1$  vanishes. All  $G_K$  are negative, since there is no atom along the z direction. The total AIS on C2 is small, because the contact term is small compared to its neighbors and the pseudocontact is the largest and of opposite sign. The sign of the contact contribution alternates between C2 and C6.

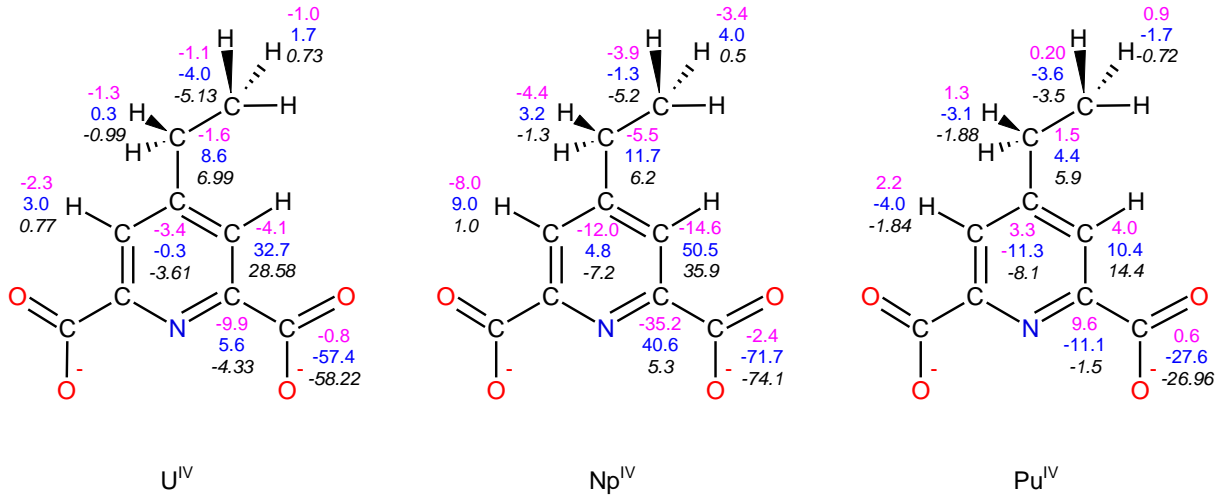


Figure 7: Pseudocontact (red), contact (blue) and total AIS (black) in ppm for  $[An^{IV}(Et-DPA)_3]^{2-}$  complexes at 298 K from temperature dependence analysis (see Table 2)

The HFC constants  $A_K^c/\hbar$  evaluated from the contact AIS and the spin-only magnetic susceptibility  $\chi_m^S$  from Table 1 using Eq. 2 are given in Table 5. One can further deduce the spin density at nucleus  $K$   $\rho^S(\mathbf{r}_K)$  according to<sup>47,48</sup>

$$\frac{A_K}{\hbar} = \frac{1}{3S} \mu_0 \mu_B \gamma_K g_e \rho^S(\mathbf{r}_K) \quad (10)$$

where  $S$  is the total electron.  $\chi_m^S$  is negative for the three actinide complexes, as a consequence of third Hund's rule. The orbital and spin contributions to the magnetization are opposite, the former being the largest, the latter is negative. Consequently,  $S$  is negative and  $S = -N/2$  where  $N$  is the number of unpaired electrons  $N=2, 3, 4$  (for  $U^{IV}$ ,  $Np^{IV}$  and  $Pu^{IV}$  respectively). The spin density at the nucleus per unpaired electron is then deduced as

$$\frac{\rho^s(\mathbf{r}_K)}{N} = -\frac{3}{2\mu_0\mu_B\gamma_K g_e} \frac{A_K}{\hbar} \quad (11)$$

Values are given in Table SI-14 and represented in Figure 8 for the  $^{13}\text{C}$  nuclei. It alternates of sign, with a decreasing envelope. The sign of  $\rho^s(\mathbf{r}_K)$  for a given carbon is the same for the three cations, and decreases from  $\text{U}^{\text{IV}}$  to  $\text{Pu}^{\text{IV}}$ . The Fermi contact shift  $\delta_K^c$  results from the combination of two mechanisms, spin delocalization and spin polarization. Spin delocalization leads to a negative spin density throughout the molecule; it is more important for the nuclei directly bonded to the paramagnetic cation and is expected to drop quickly when the number of bonds between the paramagnetic center and the observed nuclei increases. Conversely, the second mechanism propagates the spin density away from the paramagnetic center by alternating sign.<sup>49,50</sup> In the  $[\text{Yb}^{\text{III}}(\text{Et-DPA})_3]^{3-}$  complex,  $A_K/\hbar$  is mostly negative on the carbons and decreasing, which denotes the predominance of spin delocalization. In the actinide complexes, it alternates. For C1, the carbon atom of the  $\text{COO}^-$  group,  $\rho^s(\mathbf{r}_K)$  is positive, while it is only the second atom after the coordinating oxygen atom; the polarization is by far the largest on this atom. In Figure 8, it appears that the spin density decreases from  $\text{U}^{\text{IV}}$  to  $\text{Pu}^{\text{IV}}$  on all carbon atoms. This can be related to a decrease of the covalency in the early actinide series.<sup>51</sup>

Table 5: Fermi contact HFC constants  $A_K/\hbar$  (MHz) deduced from Fermi contact AIS and  $\chi_m^{S,cal}$  (Table 1) according to Eq. 2 in  $[\text{An}^{\text{IV}}(\text{Et-DPA})_3]^{2-}$  and  $[\text{Yb}^{\text{III}}(\text{Et-DPA})_3]^{3-}$ .

		C1	C2	C3	C4 <sup>A</sup>	C5	C6	H3 <sup>A</sup>	H4	H5	H6
$\text{U}^{\text{IV}}$	fit	0.70	-0.07	-0.40	0.01/0.003	-0.10	0.05	-0.14/-0.15	-0.33	-0.01	-0.08
	DFT	0.07	0.13	-0.33	0.24	-0.10	0.09				
$\text{Np}^{\text{IV}}$	fit	0.62	-0.35	-0.44	-0.26/-0.04	-0.10	0.01	-0.31/-0.31	-0.38	-0.11	-0.14
	DFT	-0.10	0.05	-0.28	0.26	-0.07	0.06				
$\text{Pu}^{\text{IV}}$	fit	0.28	0.11	-0.11	0.13/0.12	-0.05	0.05	0.16/0.16	0.09	0.12	0.07
	DFT	0.62	0.06	-0.17	0.07	-0.04	0.03				
$\text{Yb}^{\text{III}}$		-0.17	-0.06	-0.07	-0.03	-0.003	0.004	-0.02	-	0.01	0.01

<sup>A</sup>: DPA/Et-DPA

Unrestricted SR-DFT was successful to interpret HFC constants in the isotropic  $4f^7$   $\text{Gd}^{\text{III}}$ - $\text{H}_2\text{O}$  complexes<sup>28</sup> as well as  $^1\text{H}$  pNMR shifts in isostructural  $\text{Ln}^{\text{III}}$  series.<sup>29</sup> Following this line, the HFC constants were calculated using unrestricted DFT and are reported in Table 5. They are in good accordance with the values issued from the fitting procedure. To go one step further, we analyzed the Mulliken spin population using unrestricted SR-DFT with a fractional occupation of the seven  $5f$  orbitals in  $[\text{An}^{\text{IV}}(\text{DPA}/\text{Et-DPA})_3]^{2-}$  complexes. Spin polarization is well described by an unrestricted scheme by allowing the spatial parts of the  $\alpha$  and  $\beta$  orbitals to be different, while CASSCF spin densities only describe spin delocalization. The fractional occupancy in the  $5f$  orbitals in DFT resembles the state averaged CASSCF wave functions and allows for an equivalent population of all the magnetic orbitals.  $^{13}\text{C}$  AIS are mostly dominated by the Fermi contact contribution. It is worthy to mention that atomic charges and spins are not directly spectroscopic and that their evaluation according to Mulliken method depends strongly on the choice of the basis

set and provide qualitative results.<sup>52,53</sup> The Mulliken atomic spin populations  $\rho^s$  calculated with the CASSCF and unrestricted DFT methods are collected in Tables SI-16 to 18 and Figures SI-6 to 8. The CASSCF spin populations are the largest for the bonding oxygen (O1) and nitrogen atoms and become rapidly negligible after few bonds from the paramagnetic center as expected from a spin delocalization mechanism. Atomic spin populations using unrestricted DFT are much larger. DFT methods better describe the spin delocalization and furthermore, using an unrestricted scheme, they allow spin polarization mechanism. The different functionals lead to qualitatively similar results (see Figure SI-8 and Table SI-14) and the sign is in accordance with of  $\rho^s(\mathbf{r}_K)$  issued from AIS. The atomic s-orbitals have a finite radial probability density at the nucleus and are the only relevant ones for the interpretation of the contact shifts. While the spin populations in the s-orbitals  $\rho_s^s$  have the same sign as the atomic ones  $\rho^s$  with M062X, it is not the case with the other functions, especially with M06. In Figure 9, the  $\rho^s(r_K)$  values deduced from the experimental contact AIS are compared to both the atomic spin population  $\rho^s$  and the spin populations in the s-orbitals  $\rho_s^s$  calculated with M062X and we see that the three are in qualitative agreement. This alternance of sign has been described by Adamo *et al.* for aromatic free radicals,<sup>54</sup> large positive spins are obtained on the ortho (C2) and para (C4) carbons of the pyridine unit whereas the meta (C3) and ethyl (C5) have the opposite signs and reduced magnitudes, in perfect accordance with our findings. The atomic spin populations are broken down in  $\sigma$  and  $\pi$  contributions for PBE0 calculations in Table SI-19. In all cases the sign is the same in  $\sigma$  and  $\pi$  systems. They have comparable values to those obtained by a similar procedure in  $[\text{Np}^{\text{VI}}\text{O}_2(\text{Et-DPA})_2]^{2-}$  complex (See Table SI-6 in Ref<sup>23</sup>). The contributions per unpaired electron N are very similar while the bonding schemes are quite different since there are three ligands in one case, two in the other, and the oxidation state of the paramagnetic cations are different (IV and VI). In the  $[\text{Np}^{\text{VI}}\text{O}_2(\text{Et-DPA})_2]^{2-}$  complexes, the AIS were analyzed in a pure dipolar scheme. This latter analysis shows that the contact contributions are of the same order of magnitude, but in the previous study, the dipolar was largely dominant due to a large anisotropy of the susceptibility provided by the yle bond with the oxygens.

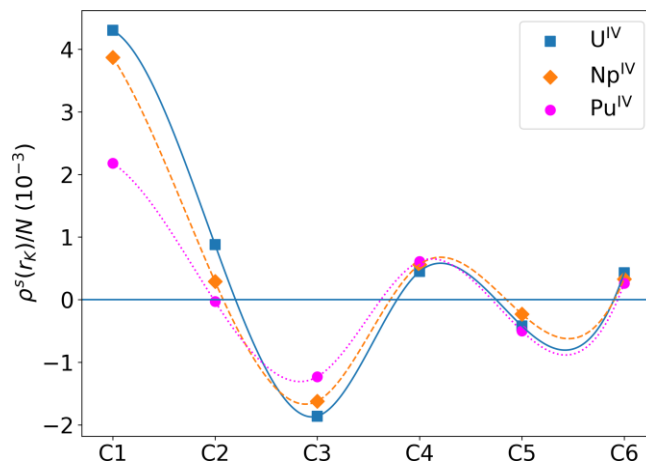


Figure 8: Spin density per unpaired electron  $\rho^s(\mathbf{r}_K)/N$  ( $10^{-3}$ ) at the  $^{13}\text{C}$  nuclei deduced from the contact AIS in  $[\text{An}^{\text{IV}}(\text{Et-DPA})_3]^{2-}$  complexes. The lines are only a guide for the eyes.

The decrease in the series of the spin density observed from the AIS is confirmed by the densities issued from uDFT calculations. This decrease in covalency was analyzed from wave-functions, Mulliken charges and electron density calculated by SO-CASPT2.<sup>30</sup> Indeed, we had shown that: (i) the nephelauxetic reduction factors decrease from U(IV) to Pu(IV). (ii) The QTAIM (Quantum Theory of Atoms In Molecules) descriptor  $|V_b|/G_b$  slightly decreases in the series. (iii) the crystal field strength parameter denotes a fast decrease. (iv) The charge analysis reveals a decrease of the ligand to metal charge transfer.

The trend of covalency in actinide series has been an object of study and controversy. The bond is mostly ionic and it has been shown that the analysis of orbital mixing and of the electron density using quantum descriptors might lead to opposite conclusions, based on spin-free DFT calculations.<sup>55,56</sup> This trend of covalency in the early actinide series has been evaluated from XANES (X-ray absorption near edge structure) spectroscopy in actinide(IV) hexachlorides<sup>57</sup>. Jung *et al.* highlighted a decreasing trend of mixing of the  $f$  orbitals with the ligands' from SO-NEVPT2 wave-functions.<sup>58</sup> Su *et al.* concluded from SF-DFT calculations that  $5f$ -orbital mixing increased from U<sup>IV</sup> to Pu<sup>IV</sup> but a recent study based on relativistic multiconfiguration calculations revealed that covalency remains the same or decreases very slightly from U to Pu. In the present series, the trend in the spin density on the carbon of the ligands issued from AIS, the analysis of the SO-CASPT2 wave function based on AILFT and QTAIM and unrestricted DFT calculations converge to conclude to a decrease of covalency from U to Pu.

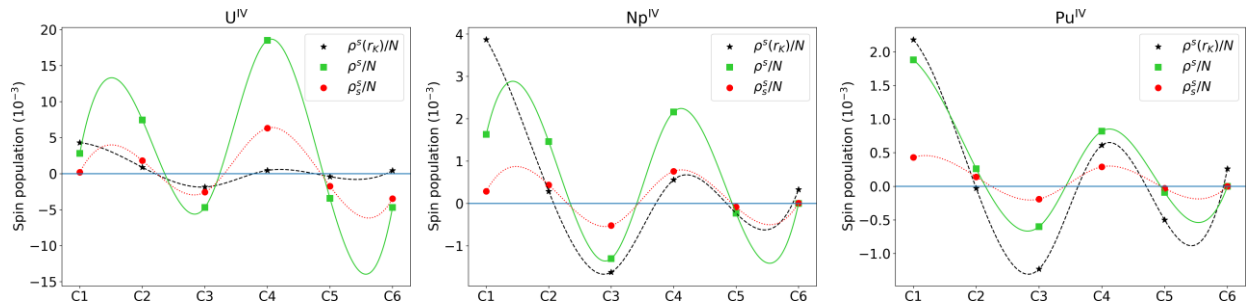


Figure 9: Spin density  $\rho^s(r_K)/N$  deduced from contact AIS, atomic spin population  $\rho^s/N$  and atomic s population electron  $\rho_s^s/N$  from unrestricted M062X at the  $^{13}\text{C}$  nuclei in the  $[\text{An}^{\text{IV}}(\text{Et-DPA})_3]^{2-}$  complexes with  $D_3$  symmetry. The lines are only a guide for the eyes.

## CONCLUSION

The paramagnetic properties of  $\text{An}^{\text{IV}}$  cations in solution were investigated by  $^1\text{H}$  and  $^{13}\text{C}$  NMR through complexes formed with dipicolinic acid derivatives (DPA and Et-DPA). The separation of the contact and dipolar contributions was achieved by the temperature dependence method. The Fermi contact contribution was described by a  $T^{-1}$  term and the dipolar one by  $T^{-1}$ ,  $T^{-2}$  and  $T^{-3}$  terms, as suggested by the thermal variation of the axial anisotropy of the susceptibility  $\Delta\chi_{ax}$  and the spin-only contribution to the average susceptibility  $\chi_m^S$ , respectively, calculated with the first principles SO-CASPT2 method. Due to the presence of the  $T^{-1}$  term in both contribution, it was necessary to inject some information from the ab initio calculation, namely the relative weight of the by  $T^{-1}$ ,  $T^{-2}$  and  $T^{-3}$  terms. This separation method has the advantage not to rely on Bleaney's theory, which already shows its limits for lanthanide complexes, and breaks down for actinide complexes, due to the larger interaction of the ligands with the metal center.

The AIS are dominated by the Fermi contact contribution, on the contrary to the  $\text{Yb}^{\text{III}}$  derivative. The coordination sphere is compact in this series, leading to a weak anisotropy of the magnetic susceptibility tensor. The dipolar contribution is consequently small. It makes the orientation of the principal axes very sensitive to any distortion. With the X-rays structures, this tensor does not follow the approximate trigonal symmetry and the dipolar chemical shifts spread over a large window, which does not suit with the experimental spectra.

The fit of the temperature dependence of the AIS allows an experimental evaluation of the axial magnetic susceptibility  $\Delta\chi_{ax}$ , those values are in good accordance with the SO-CASPT2 ones, with a change of sign between Np and Pu. The contact HFC constants  $A_K^c/\hbar$  for all NMR active nuclei can be deduced as well, using the SO-CASPT2 values for  $\chi_m^S$  and the subsequent spin densities at the nuclei. The fitted contact HFC constants are in good accordance with those calculated with unrestricted DFT. The spin densities on the  $^{13}\text{C}$  nuclei alternate in sign, denoting a predominant spin polarization mechanism, and they decrease slightly from  $\text{U}^{\text{IV}}$  to  $\text{Pu}^{\text{IV}}$ , which is the sign of a

small decrease in covalent effects. The spin densities calculated with unrestricted DFT method are in good agreement with the experimental values. This corroborate the analysis of SO-CASPT2 wave function using AILFT and QTAIM performed in a previous work.<sup>30</sup>

This study confirms that  $^1\text{H}$  and  $^{13}\text{C}$  NMR provides essential information on the paramagnetic properties and bonding mechanism in actinide complexes.

## ASSOCIATED CONTENT

**Supporting Information.** Atomics coordinates of complexes in  $D_3$  symmetry, geometric factors, plots of the experimental and SO-CASPT2 molar magnetic susceptibilities and  $\Delta\chi_{ax}^{calc}$ ,  $^{13}\text{C}$  spectra, chemical shift assignments on gHMBC and gHSQC NMR spectra, observed  $^{13}\text{C}$  and  $^1\text{H}$  chemical shift values, Mulliken atomic charges and spin densities, SO-CASPT2 energies, crystal-field parameters, fractionally occupied spin densities, calculated spin densities in the s-orbitals, linear regression fit parameters of  $^1\text{H}$  and  $^{13}\text{C}$  pNMR chemical shifts and  $\Delta\chi_{ax}^{calc}$  parameters. The following files are available free of charge.

## AUTHOR INFORMATION

### Corresponding Authors

\* E-mail: [claude.berthon@cea.fr](mailto:claude.berthon@cea.fr); [bolvin@irsamc.ups-tlse.fr](mailto:bolvin@irsamc.ups-tlse.fr)

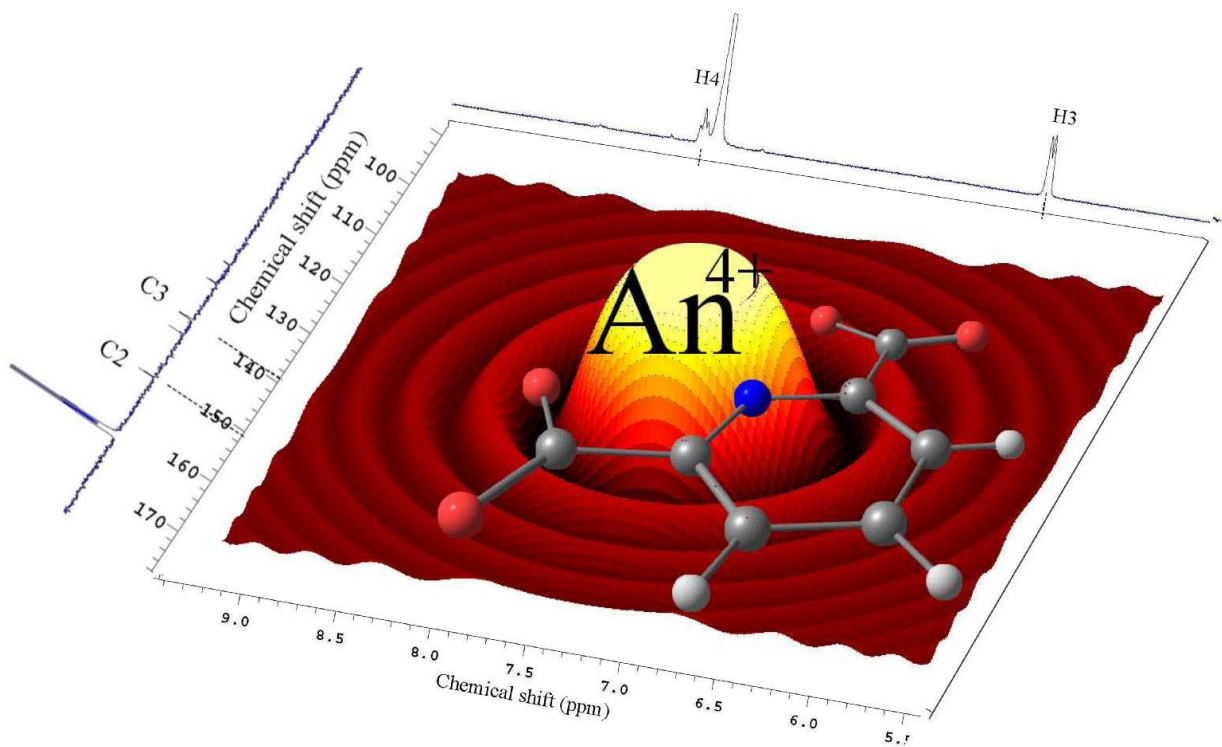
### Author Contributions

The manuscript was written through contributions of all authors. All authors have given approval to the final version of the manuscript.

### Funding Sources

This work was supported by the French ANR under convention N° ANR-17-CE06-0010.

SYNOPSIS (Word Style “SN\_Synopsis\_TOC”). If you are submitting your paper to a journal that requires a synopsis, see the journal’s Instructions for Authors for details.





## REFERENCES

- (1) Clore, M.; Potts, J. *Recent Developments in Biomolecular NMR*; The Royal Society of Chemistry, 2012. DOI: 10.1039/9781849735391. Brath, U.; Swamy, S. I.; Veiga, A. X.; Tung, C.-C.; Van Petegem, F.; Erdélyi, M. Paramagnetic Ligand Tagging To Identify Protein Binding Sites. *Journal of the American Chemical Society* **2015**, *137* (35), 11391-11398. DOI: 10.1021/jacs.5b06220. Chen, W.-N.; Nitsche, C.; Pilla, K. B.; Graham, B.; Huber, T.; Klein, C. D.; Otting, G. Sensitive NMR Approach for Determining the Binding Mode of Tightly Binding Ligand Molecules to Protein Targets. *Journal of the American Chemical Society* **2016**, *138* (13), 4539-4546. DOI: 10.1021/jacs.6b00416. Faulkner, S.; Blackburn, O. A. The Chemistry of Lanthanide MRI Contrast Agents. In *The Chemistry of Molecular Imaging*, 2014; pp 179-197. Heffern, M. C.; Matosziuk, L. M.; Meade, T. J. Lanthanide Probes for Bioresponsive Imaging. *Chemical Reviews* **2014**, *114* (8), 4496-4539. DOI: 10.1021/cr400477t. Su, X.-C.; Liang, H.; Loscha, K. V.; Otting, G.  $[\text{Ln}(\text{DPA})_3]^{3-}$  Is a Convenient Paramagnetic Shift Reagent for Protein NMR Studies. *Journal of the American Chemical Society* **2009**, *131* (30), 10352-10353. DOI: 10.1021/ja9034957. Ravera, E.; Parigi, G.; Luchinat, C. Perspectives on paramagnetic NMR from a life sciences infrastructure. *Journal of Magnetic Resonance* **2017**, *282*, 154-169. DOI: <https://doi.org/10.1016/j.jmr.2017.07.013>. Ravera, E.; Parigi, G.; Luchinat, C. What are the methodological and theoretical prospects for paramagnetic NMR in structural biology? A glimpse into the crystal ball. *Journal of Magnetic Resonance* **2019**, *306*, 173-179. DOI: <https://doi.org/10.1016/j.jmr.2019.07.027>.
- (2) Piguet, C.; Geraldes, C. F. G. C. Paramagnetic NMR Lanthanide Induced Shifts for Extracting Solution Structures. In *Handbook on the Physics and Chemistry of Rare Earths*, Gschneidner, K. A., Bunzli, J. C. G., Pecharsky, V. K. Eds.; Vol. 33; Elsevier, 2003; pp 353-463.
- (3) Miao, Q.; Nitsche, C.; Orton, H.; Overhand, M.; Otting, G.; Ubbink, M. Paramagnetic Chemical Probes for Studying Biological Macromolecules. *Chemical Reviews* **2022**. DOI: 10.1021/acs.chemrev.1c00708.
- (4) Bertini, I.; Luchinat, C. Chapter 2 The hyperfine shift. *Coordination Chemistry Reviews* **1996**, *150*, 29-75. DOI: [https://doi.org/10.1016/0010-8545\(96\)01242-8](https://doi.org/10.1016/0010-8545(96)01242-8).
- (5) Peters, J. A.; Huskens, J.; Raber, D. J. Lanthanide induced shifts and relaxation rate enhancements. *Progress in Nuclear Magnetic Resonance Spectroscopy* **1996**, *28* (3), 283-350. DOI: [https://doi.org/10.1016/0079-6565\(95\)01026-2](https://doi.org/10.1016/0079-6565(95)01026-2).
- (6) Martel, L.; Islam, M. A.; Popa, K.; Vigier, J.-F.; Colineau, E.; Bolvin, H.; Griveau, J.-C. Local Structure and Magnetism of  $\text{La}_{1-x}\text{M}_x\text{PO}_4$  ( $\text{M} = \text{Sm}, {}^{239}\text{Pu}, {}^{241}\text{Am}$ ) Explained by Experimental and Computational Analyses. *The Journal of Physical Chemistry C* **2021**, *125* (40), 22163-22174. DOI: 10.1021/acs.jpcc.1c03957.
- (7) Inagaki, F.; Miyazawa, T. NMR analyses of molecular conformations and conformational equilibria with the lanthanide probe method. *Progress in Nuclear Magnetic Resonance Spectroscopy* **1980**, *14* (2), 67-111, [https://doi.org/10.1016/0079-6565\(80\)80004-5](https://doi.org/10.1016/0079-6565(80)80004-5).
- (8) Bertini, I.; Luchinat, C.; Parigi, G.; Ravera, E. *NMR of Paramagnetic Molecules. Applications to Metallobiomolecules and Models*; Elsevier Science, 2016.
- (9) Golding, R. M.; Halton, M. P. A theoretical study of the  $^{14}\text{N}$  and  $^{17}\text{O}$  NMR shifts in lanthanide complexes. *Aust. J. Chem.* **1972**, *25*, 2577-2581, <https://doi.org/10.1071/CH9722577>.
- (10) Pinkerton, A. A.; Rossier, M.; Spiliadis, S. Lanthanide-induced contact shifts. the average electron spin polarization, theory and experiment. *Journal of Magnetic Resonance (1969)* **1985**, *64* (3), 420-425-420-425, [https://doi.org/10.1016/0022-2364\(85\)90104-0](https://doi.org/10.1016/0022-2364(85)90104-0).

- (11) Autillo, M.; Guerin, L.; Dumas, T.; Grigoriev, M. S.; Fedoseev, A. M.; Cammelli, S.; Solari, P. L.; Guillaumont, D.; Guilbaud, P.; Moisy, P.; Bolvin, H.; Berthon, C. Insight of the Metal–Ligand Interaction in f-Element Complexes by Paramagnetic NMR Spectroscopy. *Chemistry – A European Journal* **2019**, 25 (17), 4435–4451. DOI: 10.1002/chem.201805858.
- (12) Martel, L.; Magnani, N.; Vigier, J.-F.; Boshoven, J.; Selfslag, C.; Farnan, I.; Griveau, J.-C.; Somers, J.; Fanghänel, T. High-Resolution Solid-State Oxygen-17 NMR of Actinide-Bearing Compounds: An Insight into the 5f Chemistry. *Inorganic Chemistry* **2014**, 53 (13), 6928–6933. DOI: 10.1021/ic5007555.
- (13) McConnell, H. M.; Robertson, R. E. Isotropic Nuclear Resonance Shifts. *The Journal of Chemical Physics* **1958**, 29 (6), 1361–1365. DOI: 10.1063/1.1744723.
- (14) Bertini, I.; Luchinat, C.; Parigi, G. Magnetic susceptibility in paramagnetic NMR. *Progress in Nuclear Magnetic Resonance Spectroscopy* **2002**, 40 (3), 249–273. DOI: [https://doi.org/10.1016/S0079-6565\(02\)00002-X](https://doi.org/10.1016/S0079-6565(02)00002-X).
- (15) Reilley, C. N.; Good, B. W.; Desreux, J. F. Structure-independent method for dissecting contact and dipolar NMR shifts in lanthanide complexes and its use in structure determination. *Analytical Chemistry* **1975**, 47 (13), 2110–2116. DOI: 10.1021/ac60363a011. Reilley, C. N.; Good, B. W.; Allendoerfer, R. D. Separation of contact and dipolar lanthanide induced nuclear magnetic resonance shifts: evaluation and application of some structure independent methods. *Analytical Chemistry* **1976**, 48 (11), 1446–1458. DOI: 10.1021/ac50005a010. De Boer, J. W. M.; Sakkers, P. J. D.; Hilbers, C. W.; De Boer, E. Lanthanide shift reagents. II. Shift mechanisms. *Journal of Magnetic Resonance (1969)* **1977**, 25 (3), 455–476. DOI: [https://doi.org/10.1016/0022-2364\(77\)90209-8](https://doi.org/10.1016/0022-2364(77)90209-8).
- (16) Bleaney, B. Nuclear magnetic resonance shifts in solution due to lanthanide ions. *Journal of Magnetic Resonance* **1972**, 8, 91–100. Bleaney, B.; Dobson, C. M.; Levine, B. A.; Martin, R. B.; Williams, R. J. P.; Xavier, A. V. Origin of lanthanide nuclear magnetic resonance shifts and their uses. *Journal of the Chemical Society, Chemical Communications* **1972**, (13), 791b–793, 10.1039/C3972000791B.
- (17) Golding, R. M.; Pyykkö, P. On the theory of pseudocontact N.M.R. shifts due to lanthanide complexes. *Molecular Physics* **1973**, 26 (6), 1389–1396. DOI: 10.1080/00268977300102561.
- (18) Bolvin, H.; Jung, J.; Islam, M. A.; Pecoraro, V. L.; Mallah, T.; Berthon, C. Derivation of Lanthanide Series Crystal Field Parameters From First Principles. *Chemistry – A European Journal* **2019**, 25, 15112–15122, <https://doi.org/10.1002/chem.201903141>.
- (19) Elgavish, G. A.; Reuben, J. The temperature dependence of lanthanide-induced proton shifts. *Journal of Magnetic Resonance* **1974**, 16 (2), 360–361.
- (20) Stout, E. W.; Gutowsky, H. S. On the temperature dependence of lanthanide-induced NMR shifts. *Journal of Magnetic Resonance (1969)* **1976**, 24 (3), 389–398. DOI: [https://doi.org/10.1016/0022-2364\(76\)90118-9](https://doi.org/10.1016/0022-2364(76)90118-9).
- (21) Horrocks, W. D. The temperature dependencies of lanthanide-induced NMR shifts: Evaluation of theoretical approaches and experimental evidence. *Journal of Magnetic Resonance (1969)* **1977**, 26 (2), 333–339–333–339, [https://doi.org/10.1016/0022-2364\(77\)90178-0](https://doi.org/10.1016/0022-2364(77)90178-0).
- (22) McGarvey, B. R. Temperature dependence of the pseudocontact shift in lanthanide shift reagents. *Journal of Magnetic Resonance (1969)* **1979**, 33 (2), 445–455, [https://doi.org/10.1016/0022-2364\(79\)90261-0](https://doi.org/10.1016/0022-2364(79)90261-0).
- (23) Autillo, M.; Islam, M. A.; Héron, J.; Guérin, L.; Acher, E.; Tamain, C.; Illy, M.-C.; Moisy, P.; Colineau, E.; Griveau, J.-C.; Berthon, C.; Bolvin, H. Temperature Dependence of  $^1\text{H}$  Paramagnetic Chemical Shifts in Actinide Complexes, Beyond Bleaney's Theory: The  $\text{An}^{\text{VI}}\text{O}_2^{2+}$ –

- Dipicolinic Acid Complexes (An=Np, Pu) as an Example. *Chemistry – A European Journal* **2021**, (27), 1–17, <https://doi.org/10.1002/chem.202005147>.
- (24) Moon, S.; Patchkovskii, S. First-Principles Calculations of Paramagnetic NMR Shifts. In *Calculation of NMR and EPR Parameters*, 2004; pp 325-338. Kurland, R. J.; McGarvey, B. R. Isotropic NMR shifts in transition metal complexes: The calculation of the fermi contact and pseudocontact terms. *Journal of Magnetic Resonance (1969)* **1970**, 2 (3), 286–301, [https://doi.org/10.1016/0022-2364\(70\)90100-9](https://doi.org/10.1016/0022-2364(70)90100-9).
- (25) Hrobárik, P.; Reviakine, R.; Arbuznikov, A. V.; Malkina, O. L.; Malkin, V. G.; Köhler, F. H.; Kaupp, M. Density functional calculations of NMR shielding tensors for paramagnetic systems with arbitrary spin multiplicity: Validation on 3d metallocenes. *The Journal of Chemical Physics* **2007**, 126 (2), 024107. DOI: 10.1063/1.2423003. Pennanen, T. O.; Vaara, J. Nuclear Magnetic Resonance Chemical Shift in an Arbitrary Electronic Spin State. *Physical Review Letters* **2008**, 100 (13), 133002. DOI: 10.1103/PhysRevLett.100.133002. Martin, B.; Autschbach, J. Temperature dependence of contact and dipolar NMR chemical shifts in paramagnetic molecules. *The Journal of Chemical Physics* **2015**, 142 (5), 054108. DOI: 10.1063/1.4906318.
- (26) Heuvel, W. V. d.; Soncini, A. NMR chemical shift as analytical derivative of the Helmholtz free energy. *The Journal of Chemical Physics* **2013**, 138 (5), 054113. DOI: 10.1063/1.4789398.
- (27) Gendron, F.; Autschbach, J. Ligand NMR Chemical Shift Calculations for Paramagnetic Metal Complexes: 5f1 vs 5f2 Actinides. *Journal of Chemical Theory and Computation* **2016**, 12 (11), 5309-5321, <https://doi.org/10.1021/acs.jctc.6b00462>.
- (28) Esteban-Gómez, D.; de Blas, A.; Rodríguez-Blas, T.; Helm, L.; Platas-Iglesias, C. Hyperfine Coupling Constants on Inner-Sphere Water Molecules of Gd<sup>III</sup>-Based MRI Contrast Agents. *ChemPhysChem* **2012**, 13 (16), 3640-3650. DOI: 10.1002/cphc.201200417.
- (29) Rodríguez-Rodríguez, A.; Esteban-Gómez, D.; de Blas, A.; Rodríguez-Blas, T.; Botta, M.; Tripier, R.; Platas-Iglesias, C. Solution Structure of Ln(III) Complexes with Macrocyclic Ligands Through Theoretical Evaluation of <sup>1</sup>H NMR Contact Shifts. *Inorganic Chemistry* **2012**, 51 (24), 13419-13429. DOI: 10.1021/ic302322r. Castro, G.; Regueiro-Figueroa, M.; Esteban-Gómez, D.; Pérez-Lourido, P.; Platas-Iglesias, C.; Valencia, L. Magnetic Anisotropies in Rhombic Lanthanide(III) Complexes Do Not Conform to Bleaney's Theory. *Inorganic Chemistry* **2016**, 55 (7), 3490-3497. DOI: 10.1021/acs.inorgchem.5b02918.
- (30) Autillo, M.; Islam, M. A.; Jung, J.; Pilmé, J.; Galland, N.; Guerin, L.; Moisy, P.; Berthon, C.; Tamain, C.; Bolvin, H. Crystallographic structure and crystal field parameters in the [An<sup>IV</sup>(DPA)<sub>3</sub>]<sup>2-</sup> series, An = Th, U, Np, Pu. *Physical Chemistry Chemical Physics* **2020**, 22 (25), 14293-14308, 10.1039/D0CP02137G. DOI: 10.1039/D0CP02137G.
- (31) Shelkov, R.; Melman, A. Free-Radical Approach to 4-Substituted Dipicolinates. *European Journal of Organic Chemistry* **2005**, 2005 (7), 1397-1401. DOI: 10.1002/ejoc.200400637.
- (32) Kooi, J.; Weisskopf, E.; Gruen, D. M. Solubilities of Cs<sub>2</sub>UCl<sub>6</sub>, Cs<sub>2</sub>UO<sub>2</sub>Cl<sub>4</sub> and Cs<sub>2</sub>PuCl<sub>6</sub> in hydrochloric acid. *Journal of Inorganic and Nuclear Chemistry* **1960**, 13 (3), 310-312. DOI: [https://doi.org/10.1016/0022-1902\(60\)80309-0](https://doi.org/10.1016/0022-1902(60)80309-0).
- (33) Farnan, I.; Berthon, C. Applications of NMR in nuclear chemistry. In *Nuclear Magnetic Resonance: Volume 45*, Vol. 45; The Royal Society of Chemistry, 2016; pp 96-141.
- (34) Evans, D. F. 400. The determination of the paramagnetic susceptibility of substances in solution by nuclear magnetic resonance. *Journal of the Chemical Society (Resumed)* **1959**, (0), 2003-2005, 10.1039/JR9590002003.

- (35) Aquilante, F.; De Vico, L.; Ferré, N.; Ghigo, G.; Malmqvist, P.-å.; Neogrády, P.; Pedersen, T. B.; Pitoňák, M.; Reiher, M.; Roos, B. O.; Serrano-Andrés, L.; Urban, M.; Veryazov, V.; Lindh, R. MOLCAS 7: The Next Generation. *Journal of Computational Chemistry* **2010**, *31* (1), 224-247. DOI: 10.1002/jcc.21318.
- (36) Roos, B. O.; Taylor, P. R.; Sigbahn, P. E. M. A complete active space SCF method (CASSCF) using a density matrix formulated super-CI approach. *Chemical Physics* **1980**, *48* (2), 157-173. DOI: [https://doi.org/10.1016/0301-0104\(80\)80045-0](https://doi.org/10.1016/0301-0104(80)80045-0).
- (37) Andersson, K.; Malmqvist, P. A.; Roos, B. O.; Sadlej, A. J.; Wolinski, K. Second-order perturbation theory with a CASSCF reference function. *The Journal of Physical Chemistry* **1990**, *94* (14), 5483-5488. DOI: 10.1021/j100377a012.
- (38) Hess, B. A. Relativistic electronic-structure calculations employing a two-component no-pair formalism with external-field projection operators. *Physical Review A* **1986**, *33* (6), 3742-3748. DOI: 10.1103/PhysRevA.33.3742.
- (39) Heß, B. A.; Marian, C. M.; Wahlgren, U.; Gropen, O. A mean-field spin-orbit method applicable to correlated wavefunctions. *Chemical Physics Letters* **1996**, *251* (5), 365-371. DOI: [https://doi.org/10.1016/0009-2614\(96\)00119-4](https://doi.org/10.1016/0009-2614(96)00119-4).
- (40) Malmqvist, P. Å.; Roos, B. O.; Schimmelpfennig, B. The restricted active space (RAS) state interaction approach with spin-orbit coupling. *Chemical Physics Letters* **2002**, *357* (3), 230-240. DOI: [https://doi.org/10.1016/S0009-2614\(02\)00498-0](https://doi.org/10.1016/S0009-2614(02)00498-0).
- (41) Radoń, M.; Rejmak, P.; Fitta, M.; Bałanda, M.; Szklarzewicz, J. How can  $[\text{Mo}^{\text{IV}}(\text{CN})_6]^{2-}$ , an apparently octahedral  $(d)^2$  complex, be diamagnetic? Insights from quantum chemical calculations and magnetic susceptibility measurements. *Physical Chemistry Chemical Physics* **2015**, *17* (22), 14890-14902. DOI: 10.1039/C4CP04863F.
- (42) Jung, J.; Islam, M. A.; Pecoraro, V. L.; Mallah, T.; Berthon, C.; Bolvin, H. Derivation of Lanthanide Series Crystal Field Parameters From First Principles. *Chemistry – A European Journal* **2019**, *25* (66), 15112-15122. DOI: 10.1002/chem.201903141. Ungur, L.; Chibotaru, L. F. Ab Initio Crystal Field for Lanthanides. *Chemistry – A European Journal* **2017**, *23* (15), 3708-3718. DOI: <https://doi.org/10.1002/chem.201605102>.
- (43) Perdew, J. P.; Ernzerhof, M.; Burke, K. Rationale for mixing exact exchange with density functional approximations. *The Journal of Chemical Physics* **1996**, *105* (22), 9982-9985. DOI: 10.1063/1.472933 (accessed 2021/12/20).
- (44) Zhao, Y.; Truhlar, D. G. The M06 suite of density functionals for main group thermochemistry, thermochemical kinetics, noncovalent interactions, excited states, and transition elements: two new functionals and systematic testing of four M06-class functionals and 12 other functionals. *Theoretical Chemistry Accounts* **2008**, *120* (1), 215-241. DOI: 10.1007/s00214-007-0310-x.
- (45) Desreux, J. F.; Reilly, C. N. Evaluation of contact and dipolar contributions to proton and carbon-13 paramagnetic NMR shifts in axially symmetric lanthanide chelates. *Journal of the American Chemical Society* **1976**, *98* (8), 2105-2109. DOI: 10.1021/ja00424a015.
- (46) Abragam, A.; Bleaney, B. *Electron paramagnetic resonance of transition ions*; Oxford University Press, 1970.
- (47) Neese, F. Prediction of molecular properties and molecular spectroscopy with density functional theory: From fundamental theory to exchange-coupling. *Coordination Chemistry Reviews* **2009**, *253* (5), 526-563. DOI: <https://doi.org/10.1016/j.ccr.2008.05.014>.

- (48) Pell, A. J.; Pintacuda, G.; Grey, C. P. Paramagnetic NMR in solution and the solid state. *Prog. Nucl. Magn. Reson. Spectrosc.* **2019**, *111*, 1–271, <https://doi.org/10.1016/j.pnmrs.2018.05.001>.
- (49) Ruiz, E.; Cirera, J.; Alvarez, S. Spin density distribution in transition metal complexes. *Coordination Chemistry Reviews* **2005**, *249* (23), 2649–2660. DOI: <https://doi.org/10.1016/j.ccr.2005.04.010>.
- (50) Horrocks, W. D. 12 - Lanthanide Shift Reagents and Other Analytical Applications. In *NMR of Paramagnetic Molecules*, La Mar, G. N., Horrocks, W. D., Holm, R. H. Eds.; Academic Press, 1973; pp 479–519.
- (51) Kloditz, R.; Fichter, S.; Kaufmann, S.; Brunner, T. S.; Kaden, P.; Patzschke, M.; Stumpf, T.; Roesky, P. W.; Schmidt, M.; März, J. Series of Tetravalent Actinide Amidinates: Structure Determination and Bonding Analysis. *Inorg. Chem.* **2020**, *59* (21), 15670–15680, <https://doi.org/10.1021/acs.inorgchem.0c01969>.
- (52) Schindler, M.; Kutzelnigg, W. Theory of magnetic susceptibilities and NMR chemical shifts in terms of localized quantities. II. Application to some simple molecules. *The Journal of Chemical Physics* **1982**, *76* (4), 1919–1933. DOI: 10.1063/1.443165.
- (53) Barone, V. Inclusion of Hartree–Fock exchange in density functional methods. Hyperfine structure of second row atoms and hydrides. *The Journal of Chemical Physics* **1994**, *101* (8), 6834–6838. DOI: 10.1063/1.468312.
- (54) Adamo, C.; Barone, V.; Subra, R. The mechanism of spin polarization in aromatic free radicals. *Theoretical Chemistry Accounts* **2000**, *104* (3), 207–209. DOI: 10.1007/s002140000132.
- (55) Kaltsoyannis, N. Does Covalency Increase or Decrease across the Actinide Series? Implications for Minor Actinide Partitioning. *Inorganic Chemistry* **2013**, *52* (7), 3407–3413. DOI: 10.1021/ic3006025.
- (56) Kloditz, R.; Radoske, T.; Schmidt, M.; Heine, T.; Stumpf, T.; Patzschke, M. Comprehensive Bonding Analysis of Tetravalent f-Element Complexes of the Type [M(salen)<sub>2</sub>]. *Inorganic Chemistry* **2021**, *60* (4), 2514–2525. DOI: 10.1021/acs.inorgchem.0c03424.
- (57) Su, J.; Batista, E. R.; Boland, K. S.; Bone, S. E.; Bradley, J. A.; Cary, S. K.; Clark, D. L.; Conradson, S. D.; Ditter, A. S.; Kaltsoyannis, N.; Keith, J. M.; Kerridge, A.; Kozimor, S. A.; Löble, M. W.; Martin, R. L.; Minasian, S. G.; Mocko, V.; La Pierre, H. S.; Seidler, G. T.; Shuh, D. K.; Wilkerson, M. P.; Wolfsberg, L. E.; Yang, P. Energy-Degeneracy-Driven Covalency in Actinide Bonding. *Journal of the American Chemical Society* **2018**, *140* (51), 17977–17984. DOI: 10.1021/jacs.8b09436.
- (58) Jung, J.; Atanasov, M.; Neese, F. Ab Initio Ligand-Field Theory Analysis and Covalency Trends in Actinide and Lanthanide Free Ions and Octahedral Complexes. *Inorganic Chemistry* **2017**, *56* (15), 8802–8816. DOI: 10.1021/acs.inorgchem.7b00642.